UNLV | UNIVERSITY LIBRARIES

12-1-2022

Towards the Electronic Response of Carbon-Based Van Der Waals Heterostructures in a Diamond Anvil Cell

George Thomas Foskaris

TOWARDS THE ELECTRONIC RESPONSE OF CARBON-BASED VAN DER WAALS

HETEROSTRUCTURES IN A DIAMOND ANVIL CELL

By

George Thomas Foskaris

Bachelor of Science – Physics
University of Nevada, Las Vegas
2020

A thesis submitted in partial fulfillment
of the requirements for the

Master of Science– Physics

Department of Physics and Astronomy
College of Sciences
The Graduate College

University of Nevada, Las Vegas
December 2022

Thesis Approval

The Graduate College
The University of Nevada, Las Vegas

November 10, 2022

This thesis prepared by

George Thomas Foskaris

entitled

Towards the Electronic Response of Carbon-Based Van Der Waals Heterostructures in a Diamond Anvil Cell

is approved in partial fulfillment of the requirements for the degree of

Master of Science– Physics
Department of Physics and Astronomy

Ashkan Salamat, Ph.D.
Examination Committee Co-Chair

Joshua Island, Ph.D.
Examination Committee Co-Chair

Keith V. Lawler, Ph.D.
Examination Committee Member

Arya Udry, Ph.D.
Graduate College Faculty Representative

Alyssa Crittenden, Ph.D.
Vice Provost for Graduate Education &
Dean of the Graduate College

Abstract

The nanoscale regime of materials has been at the forefront of research and interest in condensed matter physics for many years. In a merger of the fields of two-dimensional (2D) materials and high pressure physics, we present an investigation of the electronic response of carbon-based, van der Waals (vdW) heterostructures in a diamond anvil cell (DAC). Combining these fields presents us with the ability to study the characteristics of such systems both optically, and through electrical transport. Properties such as conductance, band structure, and layer number are considered. The samples in this study are assembled using exfoliation and stacking techniques adapted from the 2D materials community such that atomically thin field-effect transistors can be transferred directly onto a diamond anvil surface. We discuss various techniques and tools employed to perform photolithography and electron beam deposition on the surface of diamond to make electrical connections to the heterostructures. As a benchmark, we present pressure measurements of MnS_2 using photolithographically patterned electrodes. We then present electrical measurements of graphite-gated bilayer graphene at ambient pressure and discuss avenues for future developments. We anticipate these results will lead to an entirely new platform for the investigation of high-quality heterostructures at extreme pressures.

Acknowledgements

I would like to acknowledge and thank many people who helped me throughout my development as a student of physics. Dr. Island, thank you for your extensive support and leadership. You have helped me become a better scientist, and creative technician by offering guidance and insightful intuition. I believe that from our relationship I have been able to scale many barriers of my own potential by realizing that I was capable of anything with enough time and eagerness. That my personal achievements were within reach, and while you gave room for growth, you were always present and willing to give your time. I have come to appreciate this more than words could describe. I would like to thank Dr. Salamat for encouraging me to push myself rigorously. Without the relationship we formed, I would not be here today. Thank you for seeing something in me that I did not yet see in myself. When I think back about the quality of scientist and student that I was at our meeting, and the competency that I possessed, I must say that I recognize an enormous amount of growth. Thank you both for offering me an environment to foster my potential and for helping me get through one of the most difficult times of my life. I would like to thank Dr. Lawler for always leaving a door open for me. You have consistently and humbly promoted critical thinking and a wider awareness of the science we explore to everyone that knows you. You inspire me to keep learning, reading, and appreciate the vastness of the unknown all while confidently owning the knowledge that you possess. I would also like to thank Dr. Zhou, Dr. Raja, Dr. Kwong, Dr. Chen, Dr. Martin, Dr. Selser, Dr. Cornelius, Dr. Zygelman, and Dr. Shelton for offering me years of insight into the historical

significance and physical models that represent our world. I learned so much from all of you. Thank you for your interest in my development as a student and as a physicist, for your instruction, and your enjoyment of teaching. I will miss knocking on your doors.

To my peers in the Nevada Extreme Conditions Lab, Island Lab, and the Physics department, thank you for the extended conversations on the variety of topics regarding life, research, physics, phenomena, health, and happiness. You all inspire me to become more proficient in my work as well as an excellent person outside the lab. Thank you for your friendship, the many laughs, tears, the camaraderie, and the coffee trips. I believe that each and every one of you have done, and will continue to do, great things in this life. Alex, Jasmine, Melanie, Zach, Dean, Daniel, Randy, Kristine, Justin, Joshua, Tim, Alireza, Logan, Faraz, Rachel, Trevor, Lazar, Kevin, Stanley, Kayla, Vergil, Ana, Waldo, Dylan, Christian, Sergio, Emily, Smith, Craig, Bill, Paul, and Jay... the lot of you have been role models and great friends to me. I look up to you in many ways. Your various experiences in and out of our field have ultimately helped me at various points in my life's journey that I will never forget. I truly appreciate the bonds we share, and the time we have had together.

Dedication

To my father, Thomas, whose last words to me have given me strength everyday. To my mother, Zoraida, your unconditional love has allowed me to remain wide eyed in this world. To my amazing wife, Andrea, your spirit in life inspires and fuels me wholly. To all my family, friends, and those we have lost, may the time we spend away from each other not be in vain, and may you find paradise in this life, or the next.

Table of Contents

List of Figures

Chapter 1

Introduction

Condensed matter physics has been at the forefront of science for over a hundred years and it houses a variety of disciplines and areas of expertise. Within the over-arching field, a large amount of theory, techniques, and measurement apparati have been formulated in order to explore the connections between the macroscopic and microscopic states of matter. Historically, the developments in condensed matter physics have led to a wide use of applications in modern civilization and science; where achievements have ultimately allowed for the creation and implementation of electronics, utilities in medicine, and have laid the foundation for many discoveries, such as superconductivity in 1911 by Onnes [8], and the Bose-Einstein Gas, theorized in 1925 [9] and experimentally observed in 1995 [10]. The reach of the work extends both near and far and in general, time in the field offers an abundance of questions and knowledge.

With an exposure to quantum theory and a growing competency in modern physics, one may transition between the different sub-fields of condensed matter (CM) to bridge ideas, concepts, and applications in experimental research. For example, studies taking place in the high-pressure community often investigate how solids (or fluids) physically respond when they are subjected to extreme conditions of applied pressure. The ability to measure how the energy in a material changes due to electronic, or crystallographic effects

is made possible through various spectroscopic, diffraction, and transport techniques, as well as, through varying models that predict or theorize the systems in question. In general, CM physicists are seeking to discover and understand exotic phases of matter by exploring and measuring structural and/or electronic properties of the materials in extreme conditions, and the studies can offer insight and applications in many other scientific fields like geology, chemistry, and medicine, as well as in industry. In other neighboring fields within CM, such as nanophysics, and two-dimensional (2D) physics, researchers look to discover news from the small by collecting and quantifying the response of atomically thin materials subjected to various perturbations. The 2D materials in these types of studies have reduced spatial dimensions of less than three and may be extracted through the exfoliation from a bulk parent crystal, or grown through other methods, such as atomic layer deposition or chemical vapor deposition. In general, many of the ideas and models that reside within the disciplines of CM physics, overlap with one another, and the characteristics that govern the materials in study are of apparent interest.

Two researchers, by the names of Novoselov and Geim, won the Nobel prize in physics in 2010 for their efforts in the research of graphene; they showed that a crystal of graphite could be reduced by hand via cleaving away layers from the bulk crystal to isolate an atomically thin sheet of atoms that is purely composed of carbon. These atoms bond to form graphene, and are arranged in a homogeneous, hexagonal, honeycomb-like lattice. The initial investigation by Novoselov and Geim was on the electric field effect in graphene and it eventually led to an incredible amount of experimental and theoretical research that continues to this day on graphene and many other materials [3]. Indeed, they imbued on the condensed matter community a new way to isolate atomically thin systems through the exfoliation technique itself, opening may doors and raising new questions in the 2D community. The technique remains commonly employed in 2D studies today.

As research on graphene systems grew, separate studies by Novoselov, Geim, Craciun, and Ferrari, among others, have shown that electronic properties, such as band structure,

density of states, and conductivity may be tuned with external electric fields. In time, they have also come to understand the unique characteristics of n-layered graphene systems (single, bilayer, trilayer, etc.) in response to excitations of the vibrational modes in the atomic lattice which are generated through the inelastic scattering of quasi-particle interactions attributed to photons and phonons. Ultimately, the scattering obeys the conservation of energy and the n-layered systems display their own signatures. [3, 11, 12, 13, 14, 15]. That is to say, it has been shown that the electronic properties of an n-layered graphene system are unique to one another and may be measured directly. Once again, the usefulness of the research has permeated to a large amount of researchers seeking to explore other topological properties of n-layered graphene (and other 2D materials), and their work has led to discoveries in emergent fields of twistronics [16, 17, 18], and spintronics [19, 20, 21]. In general, these studies has helped to pave the way for humankind's exploration in post-silicon nanoelectronics created new avenues of exploration in science.

It should be recognized that the reference to the works above are to illustrate the depth of interest regarding topological phenomenons accessible in and/or associated with atomically thin 2D systems. Truly, the richness of the physics therein could be the topic of many different graduate theses and the underlying effects that cloud and complicate the theory and measurements are abundant. It would be remiss to not recognize some of the many concepts associated with these systems, as it is important to highlight a wider view that everything is connected. So, as this study engages, we will consider some of the same principles and anomalies that seek to discuss the electronic characteristics of our carbon-based van der Waals (vdW) heterostructures (systems that are composed of atomically thin, heterogeneous samples that may be oriented to form devices). In this work, the terms vdW heterostructure, vdW device, stack, and atomically thin field effect transistor (ATFET) all correspond to and describe the same general structures; the terms are used interchangeably and relate to the samples in question.

In an atomically thin regime, it is possible to observe novel phenomena when subjecting vdW heterostructures to different perturbations. To measure how electronic properties change on atomically thin samples, many experiments make electrical connection to the samples to create devices. The devices are then subjected to a perpendicular electric field. This technique acts to modify the charge carrier density of the 2D materials and allows for an investigation of how the electronic properties of the materials change. The recent experiment by Jarillo-Herrero's group at MIT in 2018 [16] showed unconventional superconductivity could be measured in twisted bilayer graphene by stacking two individual layers of graphene at a "magic angle" of $\approx 1.1°$ and by tuning the magnitude of hole dopants in the atomic lattice through an external electric field. If the charge carrier density, n, fell around -1.5 electrons per unit cell, the twisted bilayer devices displayed superconductivity at temperatures near 1.7 K. Furthermore, in a separate study performed by Yankowitz et al. in 2019 showed the observation superconducting states in twisted bilayer graphene could be tuned at varying angles using both external electric field to increase hole or electron dopants, and by subjecting the vdW heterostructure to hydrostatic pressure up to a few GPa, whereby the onset of pressure acted to enhance the interlayer coupling of the bilayer graphene in an oil filled pressure cell [17]. The study concluded that the source mechanisms responsible for the superconductivity, such as electron mediated, or electron-phonon mediated, was still to be understood. They comment that higher regimes of pressure could induce shorter Moiré periodicities in the atomic lattice, making crystallographic predictions less complicated. Elsewhere, the sensitivity of interlayer coupling between adjacent layers of a vdW heterostructure has been shown to induce magnetic transitions under applied pressure holding potential applications for memory storage [22].

To connect these studies to high pressure, there have been other research in recent years that investigated the effects of pressure on graphene, and few layered graphene systems, in a diamond anvil cell (DAC) using a variety of optical and transport techniques,

all of which vary in methodology of isolating and transferring the samples. Notably, Ke et al. [23] studied a pressure-induced bandgap in trilayer graphene whereby the interlayer interaction was significant enough to induce a semimetal to semiconducting transition in the material. The onset of the semiconducting nature was measured directly through transport as a function of pressure and verified through infrared-absorption spectroscopy. The study approximately induced a 2.5 eV bandgap in the trilayer band structure at pressures near 50 GPa. The implications of the study offer applications for carbon-based electronics as previously, the largest bandgap achieved was hundreds of meV in a bilayer graphene (BLG) flake [24, 25]. Meanwhile, Tao et al., used Raman spectroscopy to trace the structural evolution of the bonding of BLG in a DAC by studying the evolution of the G and 2D peaks associated with the discrete phonon excitation modes that are found in the Stokes scattering regime near 1600 cm^{-1} and 2700 cm^{-1}, respectively [26]. They concluded that the presence of water in the sample chamber provided a pathway for functional groups to form bonds with the carbon atoms under pressures up to approximately 50 GPa. For reference, BLG is illustrated in Figure 1.1. In their study, the topside and underside of the BLG was suspended over a gold grating and loaded into a DAC. The electronic transition from sp^2 to sp^3 hybridization is characteristic of an insulating transition in the carbon allotrope of graphite. This was also observed by Smith et al. years prior in 2015, [27]. Smith's study similarly witnessed the onset of partial hydrogenation of a single layer graphene sample, grown through chemical vapor deposition on a diamond anvil surface, whereby applying pressure and heating the structure in the pressure transmitting medium (PTM) of pure hydrogen gas revealed the synthesis of an hybridized sp^3 structure C-H, called graphane. Upon decompression and annealing, the physical recoverability of the carbon-based materials in these studies may retain useful applications that could be further investigated and applied in fields exploring new electronics and hydrogen storage. In general, these studies have shown that graphene, and its pluralized constituents, have many properties that are still to be discovered when in the presence of other materials.

To date, techniques for stacking and transferring a vdW heterostructure to a diamond surface and studying its electronic response in a DAC are lacking, but the results of the many aforementioned studies provide a relevant foundation for the purpose of this research. It is evident that there is still much to learn from vdW systems in a pressurized environment, and arguably, the use of a diamond anvil cell as the instrument employed to induce pressure and strain on a vdW heterostructure may provide the ability to subject such systems to pressures up to hundreds of GPa. The ability to perform transport measurements on different vdW heterostructures in a DAC could yield an entirely new platform for the investigation of high-quality atomically thin devices at extreme pressures.
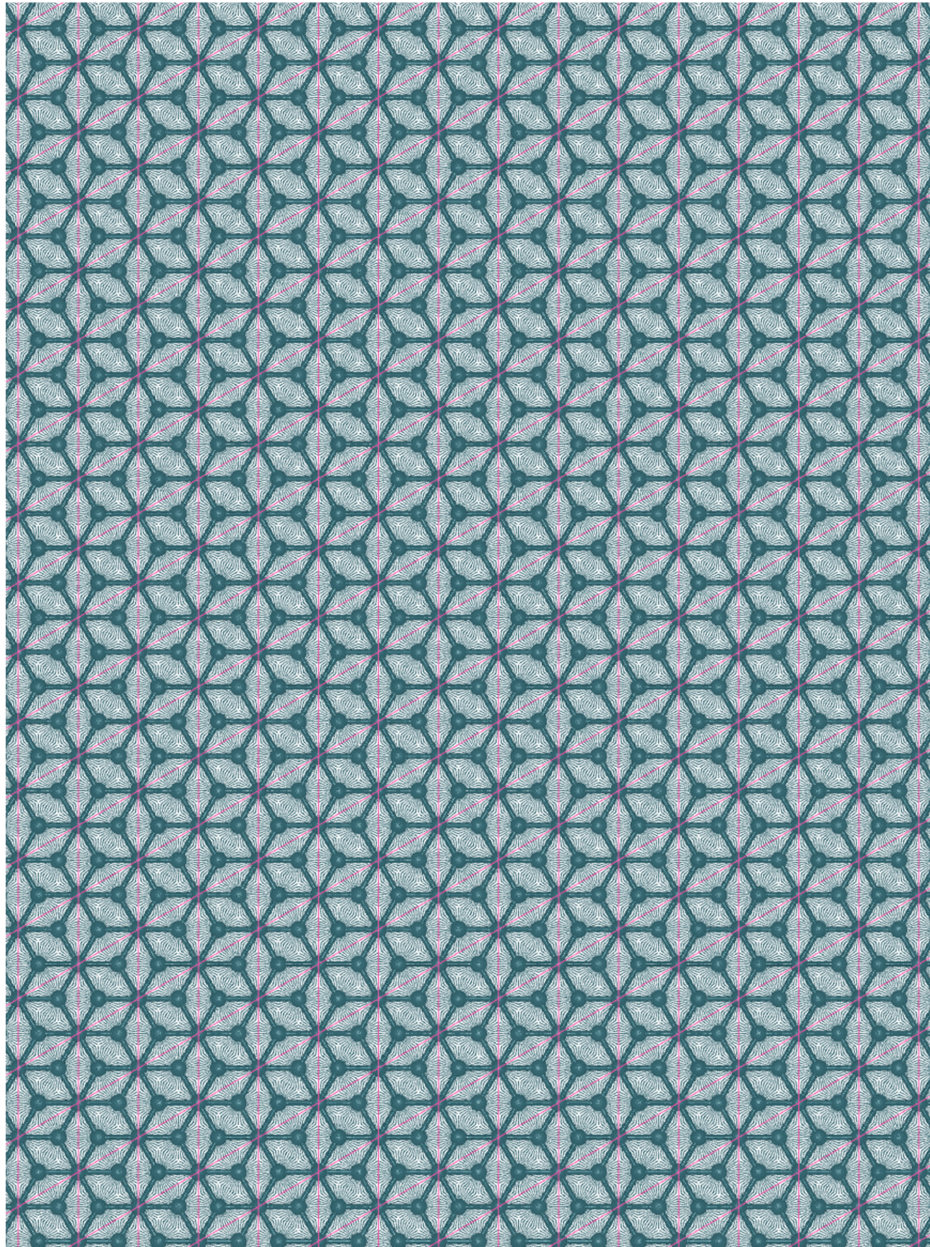
Figure 1.1: A Vesta export [1] of the Bernal (A-B) stacked bilayer graphene lattice adapted from the crystallographic results of ref. [2]. Thin pink lines found within the 2D lattice indicate the boundaries, orientation of propagation, and periodicity of the unit cell as viewed from the top, down through the layers.

Chapter 2

Theoretical Background

Carbon-based systems are in enormous variety and the significance of the element on Earth is undisputed. Interestingly, systems made of pure carbon are still of incredible importance and highly relevant in scientific research. We will come to investigate the qualities of graphene, an atomically thin allotrope of carbon which forms as individual layers of its parent structure, graphite. Graphene may be physically extracted from its bulk, parent-crystal which was physically discovered and first studied in 2004 [3]. The Nobel prize winning research on the electric field effect in exfoliated graphene by Novoselov and Geim [3] propagated new concepts and applications of graphene that have pioneered new science on electronics and nanophysics for many reasons. We begin by discussing single layer graphene as a physical material, the topics of which include presenting its corresponding crystallographic and electronic band structure.

2.1   From Graphite to Graphene - Carbon Everywhere

A crystal of graphite may be simplified to better understand the present research. Normally, graphite is considered to be a standard for hexagonal structures as it describes systems that are hexagonally close packed. It has the space group P6$_3$/mmc. The unit cell of the carbon allotrope of graphite has four atoms in it and each atom is covalently bound

to three other atoms in its plane. Figure 2.1 displays the unit cell of graphite and the ways in which one atom within the unit cell will bond to its nearest-neighbors [2, 1]. The bonding between the atoms in the same plane is of a trigonal planar geometry, periodic, and the bonds themselves display sp^2 hybridization. With the presence of periodicity, seen in Figure 2.1 (a), this creates a honeycomb-like planar lattice throughout the crystal and the individual layers are held together through van der Waals forces. The layers are most often described to be Bernal stacked [28] in an A-B-A formation, although, this could change depending on the bulk periodicity of the parent crystal; for example, rhombohedral graphite may be observed with an A-B-C type lattice stacking [29]. In addition to the two atoms found at the center of the trigonal planar bonds in each layer, it is important to see in Figure 2.1 (b), that the eight atoms along the boundary of the unit cell are sectioned such that they contribute a total of two atoms in total, one atom per layer. For Bernal stacked graphite, there are two layers in the unit cell, and thus four atoms in total. Indeed, due to the van der Waals stacking of individual layers of graphene in a graphite crystal, the physical discovery of graphene using the exfoliation technique was made possible because cleaving away the layers of a graphite crystal maintains the integrity of the planar 2D, honeycomb-like lattice. This is similar to how a graphitic pencil leaves behind a trace of graphite when writing.

As the seemingly infinite atoms in the limit of a 3-dimensional (3D) crystal of graphite begin to reach a 2-dimensional (2D) limit, the conception of graphite's structural and electronic framework begins to change. As graphene is one atomically thin layer of graphite, the fundamental lattice of graphene is therefore reduced to two atoms in the unit cell, as seen labeled in Figure 2.2 (b). Graphene, and few-layered variants of graphene, exhibit quite unique and interesting characteristics. They display differences from their bulk parent graphite, but also from one another. Here we will discuss the electronic properties of single layer and bilayer graphene.
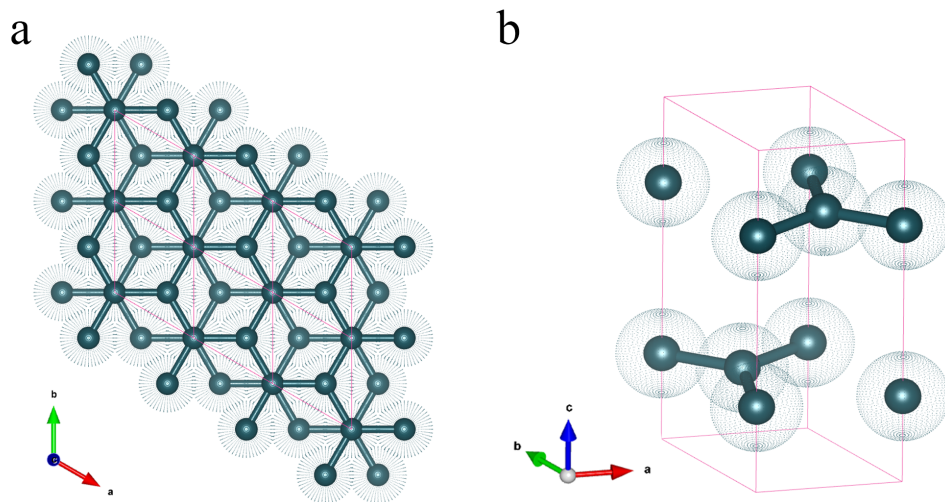
Figure 2.1: The unit cell of graphite. Graphite structure adapted from Ref. [2] in Vesta [1]. (a) Bernal stacked graphite showing six unit cells. One unit cell is denoted by a pink rhombus. The lattice may be rotated and reduced to one unit cell in space to obtain (b). (b) A 3D representation of one unit cell displayed as a rhombohedron - each atom on the boundary or interior to the unit cell is displayed. The lattice displacement vectors are $\left\langle \vec{a}, \vec{b}, \vec{c} \right\rangle = \langle 2.47, 2.47, 6.80 \rangle$ Å.

2.1.1 Electronic Characteristics of Single Layer Graphene

The electronic configuration of atomic carbon is $1s^2 2s^2 2p^2$. In the allotrope of graphite, three of the four electrons in the valence band display sp^2 hybridization and form very strong σ-bonds with the nearest-neighboring atoms. The fourth electron is primarily responsible for graphene's unique electronic qualities, such as conductivity, and electron mobility, and can be described as a massless Dirac Fermion [30]. The superposition wavefunction for the electrons forming the co-planar σ-bonds may be described as

$$\Psi_\sigma = \frac{1}{\sqrt{3}} \left(\psi(2s) + \sqrt{2}\psi(\sigma_i 2p) \right) \tag{2.1}$$

such that σ_i, where $i = 1, 2, 3$, denotes the direction of the three bonds to the in-plane nearest-neighbors, and $(2s)$, $(2p)$ denote the corresponding electron orbital, respectively. However, the fourth electron forms a π-bond out of the planar lattice, and is described to be in the $2p_z$ state. The co-planar covalent bonds do not contribute to the conductivity in graphene [28].

To understand the electronic characteristics of graphene, we may first describe the lattice vectors associated with the fundamental cell. Figure 2.2 (a) displays an extended lattice of pristine graphene in its ground state and (b) indicates the sublattices therein. We may recall that the unit cell for a graphene consists of two atoms, A and B; in panel (b), they are differentiated by green and red atoms, respectively. In Figure 2.2 (b), the shortest interatomic distance may be described by the nearest-neighbor vectors, $\boldsymbol{\delta_i}$, such that $i = 1, 2\,3$, whereby they connect atoms of different sublattices (displayed in different color) $[B \rightarrow A]$, and are given by

$$\vec{\delta_1} = -a\langle 1,0 \rangle \quad \vec{\delta_2} = \frac{a}{2}\left\langle 1, \sqrt{3} \right\rangle \quad \vec{\delta_3} = \frac{a}{2}\left\langle 1, -\sqrt{3} \right\rangle. \tag{2.2}$$

The atomic distance between nearest-neighboring carbon atoms, $[A \rightarrow B]$, is $a = 1.42$ Å[30]. With the nearest-neighbor distance on hand, we may describe the next
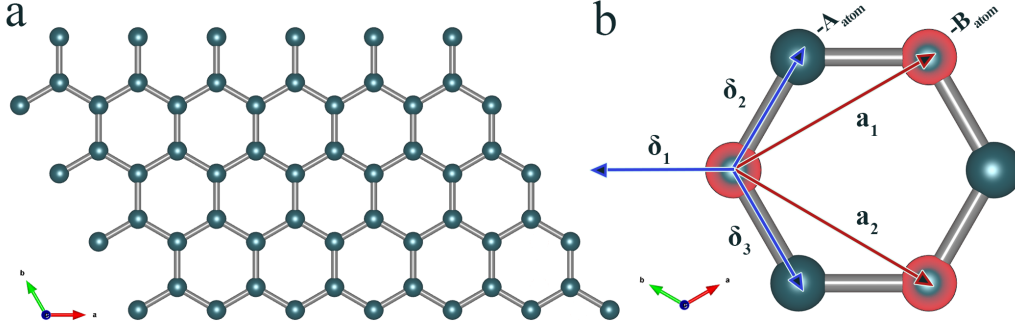
Figure 2.2: Graphene is an atomically thin layer of graphite. (a) A sheet of graphene illustrating the honeycomb-like lattice structure. (b) The intraplanar atomic distance vectors from ref. [3], whose associated displacement vectors may be seen in Equations 2.3 and 2.2. Crystal structure adapted from ref. [2] using Vesta [1].

nearest-neighbor distances with the red lattice vectors, $\mathbf{a_j}$, which connect atoms of a similar sublattice (displayed with similar color) $[B \rightarrow B]$, given by

$$\vec{a_1} = \left\langle \frac{3a}{2}, \frac{\sqrt{3}a}{2} \right\rangle \qquad \vec{a_2} = \left\langle \frac{3a}{2}, -\frac{\sqrt{3}a}{2} \right\rangle. \tag{2.3}$$

Using the tight-binding approximation for graphene [28], the electron in the $2p_z$ orbital, may be described using Bloch's theorem through the superposition wavefunction of the A and B sublattices in the form of

$$\Psi_{p_z}(\mathbf{r}) = \sum_{A_i} e^{i\mathbf{k}\cdot\delta_{\mathbf{A_i}}} X(\mathbf{r} - \delta_{\mathbf{A_i}}) + \lambda \sum_{B_j} e^{i\mathbf{k}\cdot\delta_{\mathbf{B_j}}} X(\mathbf{r} - \delta_{\mathbf{B_j}}). \tag{2.4}$$

Defining the units therein, the sum over the A (or B) sublattice includes all the lattice points that are formed through a primitive translation from A (or B) and has a phase factor whereby $\mathbf{k} \cdot \boldsymbol{\delta_{Ai}}$ (and $\mathbf{k} \cdot \boldsymbol{\delta_{Bj}}$) is the projection of the momentum, $\mathbf{k}$, along the ith nearest-neighbor displacement, $\boldsymbol{\delta_i}$, λ is an arbitrary prefactor, and $X(\mathbf{r})$ is a normalized

wavefunction of the $2p_z$ orbital. The index i and j on the A and B atomic species correspond to discrete lattice displacements from the A and B sublattice sites. Figure 2.3(b) displays the Brillouin zone for single layer graphene and the associated reciprocal lattice vectors in momentum space, which may be described in the form of

$$\vec{b_1} = \frac{2\pi}{3a}\left\langle 1, \sqrt{3} \right\rangle \qquad \vec{b_2} = \frac{2\pi}{3a}\left\langle 1, -\sqrt{3} \right\rangle. \tag{2.5}$$

If we assume that there is not an overlap between the nearest-neighboring π-bonds in the $2p_z$ orbital, then we may conclude that the normalized wavefunctions associated with the A and B sublattices are orthogonal to one another, such that

$$\int X^*(\mathbf{r} - \delta_{\mathbf{Ai}})X(\mathbf{r} - \delta_{\mathbf{Bj}})d\mathbf{r} = 0. \tag{2.6}$$

On the contrary, the Kronecker delta is formed if and only if the ith and j^{th} sublattices are of the same index and of the species, i.e. a complete overlap, such that

$$\int X^*(\mathbf{r} - \delta_{\mathbf{Ai}})X(\mathbf{r} - \delta_{\mathbf{Aj}})d\mathbf{r} = \delta_{ij}. \tag{2.7}$$

The orthogonality condition and tight-binding approximation will eventually allow us to simplify the Hamiltonian operator as we apply it to the wavefunction seen in Equation 2.4. The associated Hamiltonian for an arbitrary momentum in reciprocal space may be seen in the form of

$$\hat{H} = H_o + \Delta U = \gamma_o \sum_{<i,j>} \left(a_i^\dagger \hat{b}_j + \mathbf{H.C.} \right) + \Delta U. \tag{2.8}$$

For now, the Hamiltonian operator in Equation 2.8 acts to create, and annihilate, an electron on sublattice sites A, and B, respectively via $a_i^\dagger$, and $\hat{b}_j$. The Hermitian conjugate, $\mathbf{H.C.}$, is also possible, which acts to create, and annihilate, an electron on sublattice sites B, and A, respectively via $b_j^\dagger$, and $\hat{a}_i$. The Coulombic potential, ΔU, apparent to the

electron in the $2p_z$ orbital from its host nucleus is taken to be negligible, and the prefactor, γ_o is an electron hopping parameter associated with the energy required to hop between nearest-neighbor lattice sites. γ_o is important in the approximation of the electronic band structure of graphene and may be approximated such that $\gamma_o = 2.8\ eV$ [30]. It should be mentioned that with sufficient energy, it is possible that an electron may hop to the next nearest-neighbor, i.e. hopping to a similar sublattice species, but the correction presented is only shown to first order.

Conveniently, the eigenstate of this Hamiltonian was previously seen in Equation 2.4 and may be further understood through Bloch's theorem which states that the solutions to Schrödinger's equation for a system in a periodic potential are in the form of plane waves that are modulated by some periodic function. In this way, the $X(\mathbf{r})$ functions modulate the corresponding plane wave, and $\mathbf{k} \cdot \delta_{\mathbf{A_i}}$ (as well as $\mathbf{k} \cdot \delta_{\mathbf{B_i}}$) projects the plane wave's momentum into the direction of the nearest-neighbor. Therefore, making use of this solution, we may write the associated time-independent Schrödinger equation as

$$\hat{H}\Psi_{p_z}(\mathbf{r}) = \epsilon\Psi_{p_z}(\mathbf{r}). \tag{2.9}$$

To describe the electronic band structure of graphene within the tight-binding approximation to first order, we may find the expectation value of the Hamiltonian operator on the wave-function of the $2p_z$ electron and its complex conjugate [28, 31] in the form of

$$\epsilon(k) = \left\langle \Psi_{p_z}^\dagger | \hat{H} | \Psi_{p_z} \right\rangle \tag{2.10}$$

which can be shown to be equivalent to the energy dispersion in momentum space, i.e. the electronic band structure, displayed in Figure 2.3 (a), such that

$$\epsilon_\pm(k) = \pm\gamma_o\sqrt{3 + 4cos\left(\frac{\sqrt{3}ak_x}{2}\right)cos\left(\frac{ak_y}{2}\right) + 2cos(ak_y)}. \tag{2.11}$$

The energy band structure for the π-band electrons in the Brillouin zone may be seen
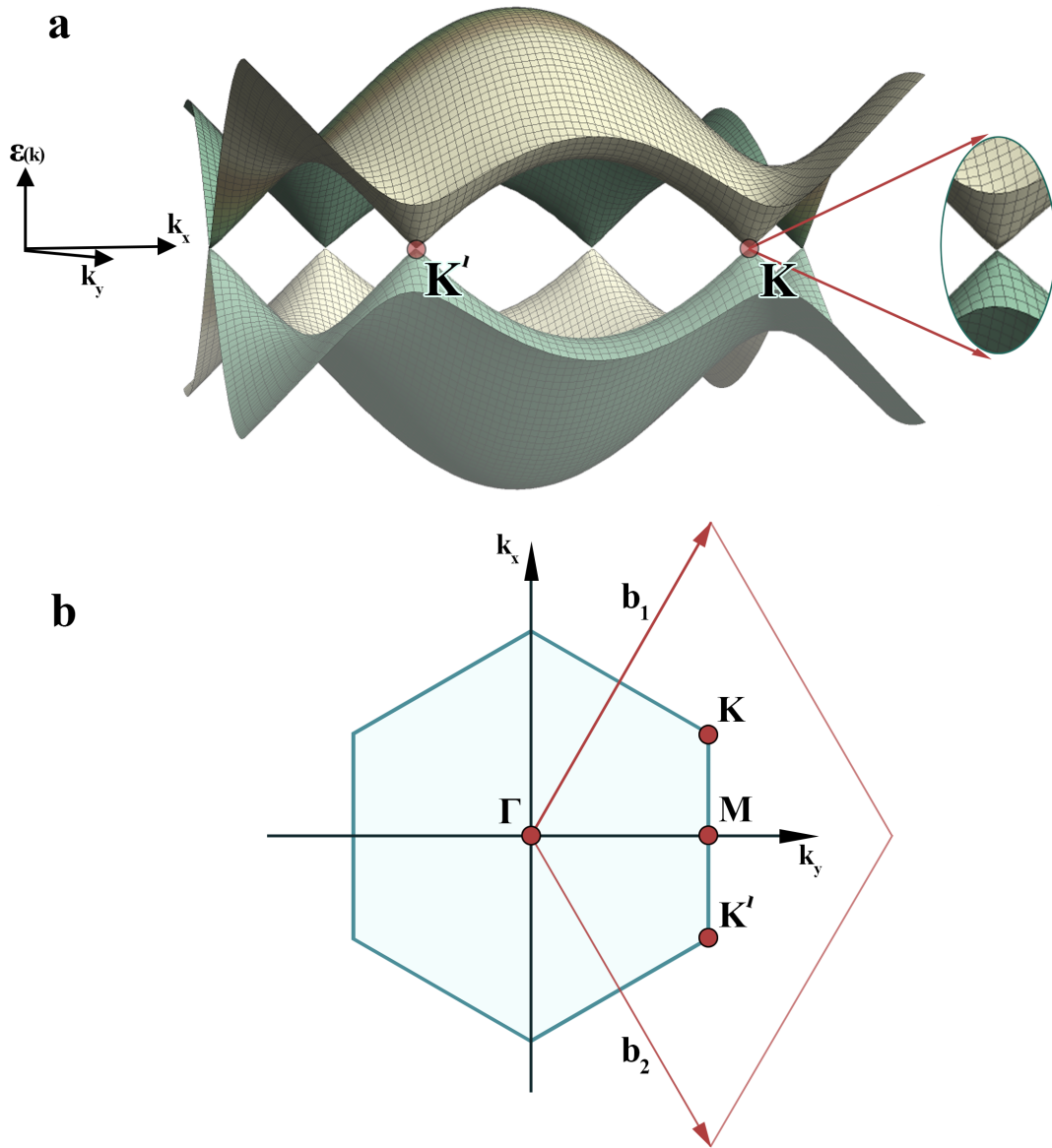
Figure 2.3: The energy-momentum dispersion and lattice vectors in the Brillouin zone for single layer graphene.(a) A plot of the positive and negative energy-momentum dispersion of the electronic band structure of single layer graphene. The arrows on the right highlight the high symmetry points found at the K and K' positions in reciprocal space. Notice the expanded energy dispersion on the right hand side is linear through the Dirac Point found at $\epsilon(k) = 0$, a unique signature of single layer graphene and the byproduct of a relativistic fermion. (b) A Brillouin zone primitive cell indicating the corresponding high symmetry points found in reciprocal space.

in Figure 2.3 (a). The result offers an illusive visualization at the phenomena that has made graphene a top contender in modern material research. The heart of the matter falls on the analysis of the energy dispersion near the $\pm$K and $\pm$K' points, which has been expanded on the right hand side in Figure 2.3 (a). The figure illustrates the dispersion of the valence and conduction bands near the Fermi level. The valence and conduction bands connect through the K (and K') points with a linear continuity through the Fermi level in energy space. The point at which they cross is termed the Dirac Point and the bands at these points are half filled - this is due an electron-hole symmetry, which is a quality in graphene that allows for its remarkable characteristics. As we explore the material qualities of graphene, it is important to recognize that if the dispersion at the $\pm$K and $\pm$K' points is linear, then we will want to come to understand the mechanisms within the tight-binding approximation that make it so.

If there is a degeneracy at the $\pm$K and $\pm$K' points of the Brillouin zone due to the electron-hole symmetry, and the energy at that point is described by the Fermi level, we may write the energy, ϵ, such that

$$\epsilon_\pm(K) = \epsilon_\pm(K') = 0 \ eV. \tag{2.12}$$

To obtain an expression for the dispersion near the K and K' points of the Brillouin zone, we need to recognize the electron-hole symmetry near those points. First, we describe the Hamiltonian of Equation 2.8 in matrix form, such that

$$\hat{H} = \gamma_o \begin{pmatrix} 0 & \sum_i e^{i\mathbf{k}\cdot\delta_\mathbf{i}} \\ \sum_j e^{i\mathbf{k}\cdot\delta_\mathbf{j}} & 0 \end{pmatrix}. \tag{2.13}$$

Now, to account for the electron-hole symmetry, we may expand this Hamiltonian in such a way that it increases the basis states that correspond to both the A and B sublattices at the K and K' points in the Brillouin zone. If we create vectors in reciprocal space that lead from the gamma point in the Brillouin zone to the K and K' positions and define them as

Fermi point vectors, $\mathbf{K}$ and $\mathbf{K'}$, we may expand the Hamiltonian seen in Equation 2.13, such that

$$\hat{H} = \frac{\sqrt{3}}{2}a\gamma_o \begin{pmatrix} 0 & ipe^{-i\theta} & 0 & 0 \\ -ipe^{i\theta} & 0 & 0 & 0 \\ 0 & 0 & 0 & ipe^{i\theta} \\ 0 & 0 & -ipe^{-i\theta} & 0 \end{pmatrix}. \tag{2.14}$$

Here, the Hamiltonian basis has been expanded, and through substitution of the Pauli spin matrices, the 4x4 matrix may be represented as the projection of the Pauli spin vectors in x and y, $\boldsymbol{\sigma} = (\sigma_x, \sigma_y)$ on the momentum, $\mathbf{p} = \mathbf{K}^{(')} - \mathbf{k}$, such that

$$\vec{K} = \left\langle 0, \frac{4\pi}{3a} \right\rangle \qquad \vec{K'} = \left\langle 0, -\frac{4\pi}{3a} \right\rangle \tag{2.15}$$

which reduces Equation 2.14 into

$$\hat{H} = \frac{\sqrt{3}}{2}a\gamma_o \begin{pmatrix} \boldsymbol{\sigma} \cdot \mathbf{p} & 0 \\ 0 & -\boldsymbol{\sigma} \cdot \mathbf{p} \end{pmatrix}. \tag{2.16}$$

The prefactor in Equation 2.16 is not arbitrary, it is equal to the Fermi velocity, such that

$$v_F = \frac{\sqrt{3}}{2}a\gamma_o \tag{2.17}$$

and holds a value to the order of $v_F = 10^6 \ m/s$ [28, 32, 31]. Making use of the de Broglie momentum $p = h/\lambda$ and the wavevector notation $\lambda = 2\pi/k$, the energy dispersion associated with the momentum at the K and K' points can be described by the linear relationship of energy-momentum dispersion

$$\epsilon(k) = \pm\hbar v_F k. \tag{2.18}$$

This is quite a unique property for the charge carriers in graphene, which have been

described as massless Dirac fermions [11]. The phenomena arises in the 2D limit of the structure near the Dirac point and has been theorized and observed to have unique characteristics such as an effective zero rest mass (within limitation), quantized conductance, and an approximation that the electron is a relativistic particle. To highlight the differences presented, we may look to discern the differences between this relativistic type of dispersion and that of a classical particle, where we may recognize that energy is commonly proportional to the square of the momentum, p^2, such that

$$E(p) = \frac{p^2}{2m_e} \quad , \quad p = \sqrt{2m_e E} \quad , \quad v = \sqrt{\frac{2E}{m_e}} \qquad (2.19)$$

where the effective electron mass is m_e, and velocity of that particle is v. However, returning to Equation 2.17, we will notice once again that the velocity is constant and does not depend on a classical energy-momentum relation. Once again, the dispersion at the K and K' points is linear in momentum, and in comparison to a classical particle, we have truly encountered a relativistic phenomenon.

2.1.2 Electronic Characteristics of Bilayer Graphene

Bilayer graphene also displays electron-hole symmetry at the K and K' points of the Brillouin zone; however, the energy dispersion, as a function of momentum, k, is parabolic within an unperturbed, low-energy approximation. In the absence of an external electric field, the conduction and valence bands meet at the Dirac-like K (K') points in momentum-space, but given the layered structure of the 2D system, the electron hopping parameters are expanded to include the possibility of interplane hopping, which may be visualized in Figure 2.4. The associated Hamiltonian, within the tight-binding approximation [30], may be written

$$\hat{H} = - \gamma_o \sum_{<i,j>} \sum_{m,\sigma} \left(a^\dagger_{m,i,\sigma} b_{m,j,\sigma} \right)$$
$$- \gamma_1 \sum_{j,\sigma} \left(a^\dagger_{1,j,\sigma} a_{2,j,\sigma} \right)$$
$$- \gamma_4 \sum_{j,\sigma} \left(a^\dagger_{1,j,\sigma} b_{2,j,\sigma} + a^\dagger_{2,j,\sigma} b_{1,j,\sigma} \right) \tag{2.20}$$
$$- \gamma_3 \sum_{j,\sigma} \left(b^\dagger_{1,j,\sigma} b_{2,j,\sigma} \right).$$

In Equation 2.20, the first term is similar to what we saw previously for single layer graphene with the addition of the m index which identifies the upper or lower layer of Bernal stacked BLG. The creation and annihilation operators act on the corresponding sublattices of A and B, with hopping energy, γ_o, respectively. The second, third, and fourth terms arise from interplane hopping, whereby the electron sites found at alternating A and B sublattices of BLG will operate to either create or destroy electrons found at the sublattice sites between adjacent layers. γ_1 is the hopping parameter between sites found directly above and below A-to-A sublattice sites. γ_3 corresponds to interlayer hopping between sublattice sites of B-to-B, and γ_4 corresponds to hopping between sublattice sites of different layers, A-B. In graphite, the associated gamma parameters are approximately $\gamma_1 = 0.4 \ eV$, $\gamma_3 = 0.3 \ eV$, and $\gamma_4 = 0.04 \ eV$ [4, 5]; the magnitudes of which reduce as the distance between sites is increased, indicating there is reduced probability that the associated electron will move significantly further away from the lattice sites in its immediate proximity. All the terms display σ in the sum index to identify the electron spin of the given particle [30].

The band structure, or energy dispersion, of bilayer graphene is naturally more complicated. If we assume that the hopping parameter corresponding to the longest displacement, γ_4, is trivial, then the effective Hamiltonian matrix associated with Equation 2.20 may be written as
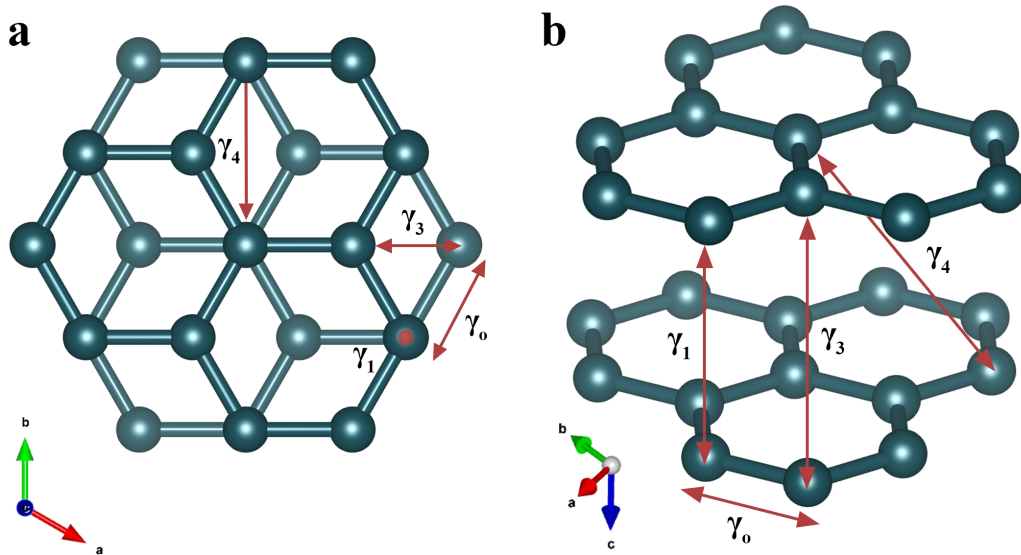
Figure 2.4: The spatial orientation of the electron hopping parameters γ_o, γ_1, γ_3, and γ_4 in Bernal stacked bilayer graphene [4, 5]. (a) The top and (b) offset side view of a BLG structure adapted from ref. [2], in Vesta [1].

$$\hat{H} = \begin{pmatrix} -V & v_F k & 0 & 3\gamma_3 a k^* \\ v_F k^* & -V & \gamma_1 & 0 \\ 0 & \gamma_1 & V & v_F k \\ 3\gamma_3 a k & 0 & v_F k^* & V \end{pmatrix}. \tag{2.21}$$

In Equation 2.21, the momentum, k, is a complex number such that $k = k_x + ik_y$. The Hamiltonian matrix itself seems quite complicated to diagonalize, but it may be approximated even further if an assumption is made that the interlayer potential, V, is zero. Ignoring the potential between the layers, as well as the hopping parameter associated with γ_4, the matrix reduces to a more manageable form, such that

$$\hat{H} = \begin{pmatrix} 0 & \frac{v_f^2 k^2}{\gamma_1} + 3\gamma_3 a k^* \\ \frac{v_f^2 k^2}{\gamma_1} + 3\gamma_3 a k & 0 \end{pmatrix}. \tag{2.22}$$

We must recognize that the assumption that the interlayer potential, V, is equal to zero will not be held valid if an external potential field is applied to the bilayer system, as the internal electrochemical potential will couple to the external field. Indeed, it is due to this internal potential between the layers of BLG that allows a band-gap to open between the valence and conduction bands at the K and K' points when subjected to an external electric field [33].

Through the simplified assumptions presented, we are able to obtain the energy dispersion for bilayer graphene. Similar to single layer graphene, the valence and conduction bands meet at the Fermi-energy neatly approximating bilayer graphene to be semi-metallic; however, as the parabolic-bands meet at the K and K' points of the Brillouin zone, the energy-momentum dispersion may be approximated in the form of

$$\epsilon(k) = \pm\frac{v_f^2 k^2}{\gamma_1}. \tag{2.23}$$

Within the approximation, this form of the energy dispersion is parabolic near the charge

neutrality point at K and K', but the most noticeable difference between it and single layer graphene is that the dispersion relation is no longer linear. Once again, we emphasize the unique quality of graphene's electronic dispersion in a 2D limit. Though here, we will find that the tuneability of the band structure in bilayer graphene may allow for the control of desired electronic effects employed by common semi-conductors, like opening and closing a band gap in a material through perpendicular electric field effects (gating), or promoting conduction of a material by supplying dopants to lattice; however, doing so requires us to reassess the system with the electronic interlayer coupling and perpendicular perturbation if we wish to obtain a more accurate representation of a bilayer graphene system in question.

At this point, we may begin to have a general understanding of how the energy dispersion of bilayer graphene may behave when measured through a mesoscopic device of an atomically thin vdW heterostructure. Once again, it is important to recognize that the aforementioned theory is within the tight binding approximation, and that the real, physical effects of the systems in study, may vary depending on a variety of factors that are not currently presented, such as disorder in the lattice, and the effects of pressure - which would certainly create the need to develop a more complicated Hamiltonian to account for effects like interlayer coupling, or spin-orbit coupling through the reduction of interplane spacing. For a crystal of graphite, the separation distance between planes is approximately 3.4 Å[28]. Furthermore, depending on the pressure cell and the PTM employed in a pressure study, other potential inclusions to describe system under pressure could lead to exploring the effects of deviatoric stress which may become apparent through varied strain on the sample in the form of a stress tensor, and/or the possibility for the PTM to intercalate in between the layers of the vdW heterostructure, if applicable. These effects have been studied in other 2D systems, although the theory that describes the systems is not abundant [34, 35, 36], and is not presented here as this study did not successfully engage pressure on any vdW heterostructures.

Chapter 3

Methods

This chapter focuses on the applied methodology to create an electrical circuit for measurements of vdW heterostructures in a diamond anvil cell. It highlights the importance of the intermediary stages of processing and fabrication by discussing the techniques and tools employed to build an instrument that is capable of both optical and transport measurements in an extreme environment. The focus of the section is to provide a clear and concise prescription so that it may be applied by others. To obtain practical samples of 2D materials, orient and stack them on top of one another, and transfer them to a diamond anvil substrate, we begin by isolating and identifying the samples used to create vdW heterostructures and the required metrics for transferring them to a DAC. Thereafter, the electrical connection is made to the sample using photolithography and electron beam deposition and may be studied once the final connection from the microscopic to the macroscopic system for experimentation is made.

3.1   The Diamond Anvil Cell

To apply pressure to a sample chamber of desired geometry, a diamond anvil cell (DAC) may be employed. DACs have been considered one of the most important tools to the field of high-pressure physics since their invention in 1959 [37, 38]. There have been
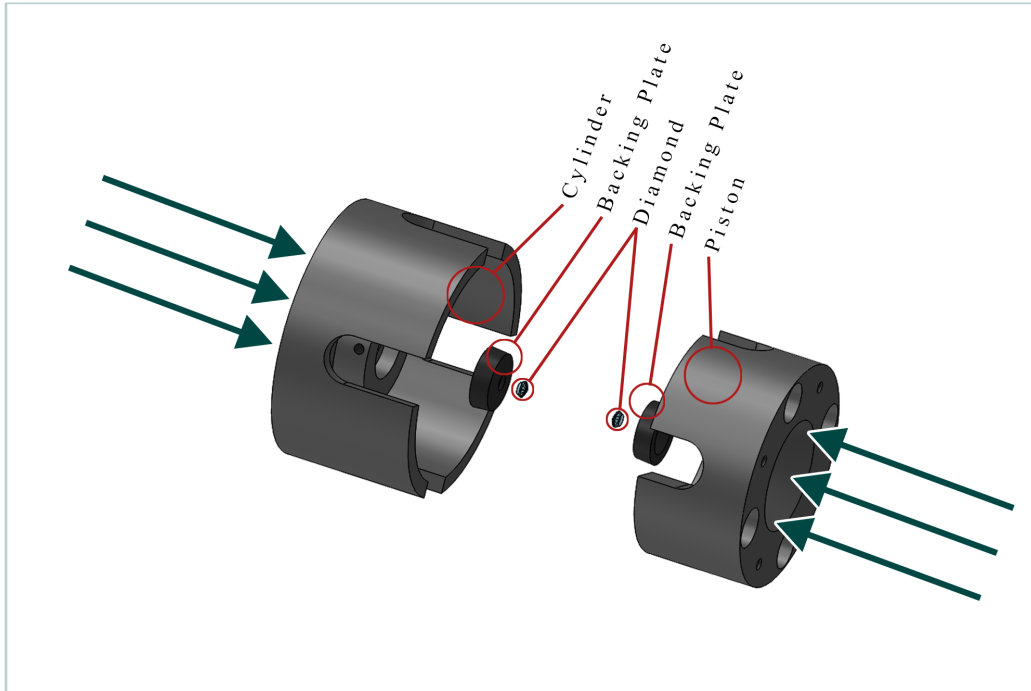
Figure 3.1: An exploded view of a PEAS DAC. Arrows indicate the direction of uni-axial compression in the pressure cell. The piston fits into the cylinder with a tight tolerance and may be aligned using a fiducial mark. Once aligned, the diamonds of the piston, and of the cylinder, are set to their respective backing plates using Loctite™ Stycast 2850 and Catalyst 9. The backing plates fit directly into the internal chassis of the piston, or of the cylinder, and are set in place using hex screws.

many types of DACs that have been created, each with their own strengths and purpose in application. The DAC used for the majority of the presented research is of the Paul Ellison Ashkan Salamat (PEAS) type. A PEAS DAC, as seen in Figure 3.1, is a steel pressure cell consisting of two halves, each of which is situated with a concentric diamond mounted to a backing plate at its interior's center. The halves forming the chassis of the PEAS DAC obtain the names, "Piston," and, "Cylinder," as the former fits into (and translates through) the latter with a tight tolerance. The assembly is compressed together until the concentric diamonds make contact with a desired gasket to create a pressure chamber that can be used to study materials and samples at extreme conditions. The distance between the diamond faces may be to the order of tens of microns.

3.1.1   Seating the Diamonds & Assembly of a DAC

The diamonds employed in a DAC are typically of the highest quality. They are often lab-grown and contain a high level of carbon purity with reduced impurities (nitrogen, boron). The form in which the two opposing diamonds are employed in a pressure cell may be actualized when the tips of the diamonds are shaved down and flattened to create a planar substrate regions that are perpendicular to the direction of uni-axial compression. The corresponding area, named the "culet," may be chosen at various diameters depending on the desired pressure regimes the experiment is seeking to explore. Reducing the diameter allows for higher pressure regimes to be explored, recalling that algebraically, pressure is described as the magnitude of an applied perpendicular force per unit area, $P = F/A$. There are also various cuts of diamonds that may be used, each with their own desirable characteristics that may be sought for experiment. The opposing tips of the diamonds in a DAC must be seated and aligned before they may come together to form a functional pressure cell.

Seating and alignment is performed in the same session. The chosen diamond is placed on top of a cylindrical tungsten carbide backing plate and held in place by a conical sheath
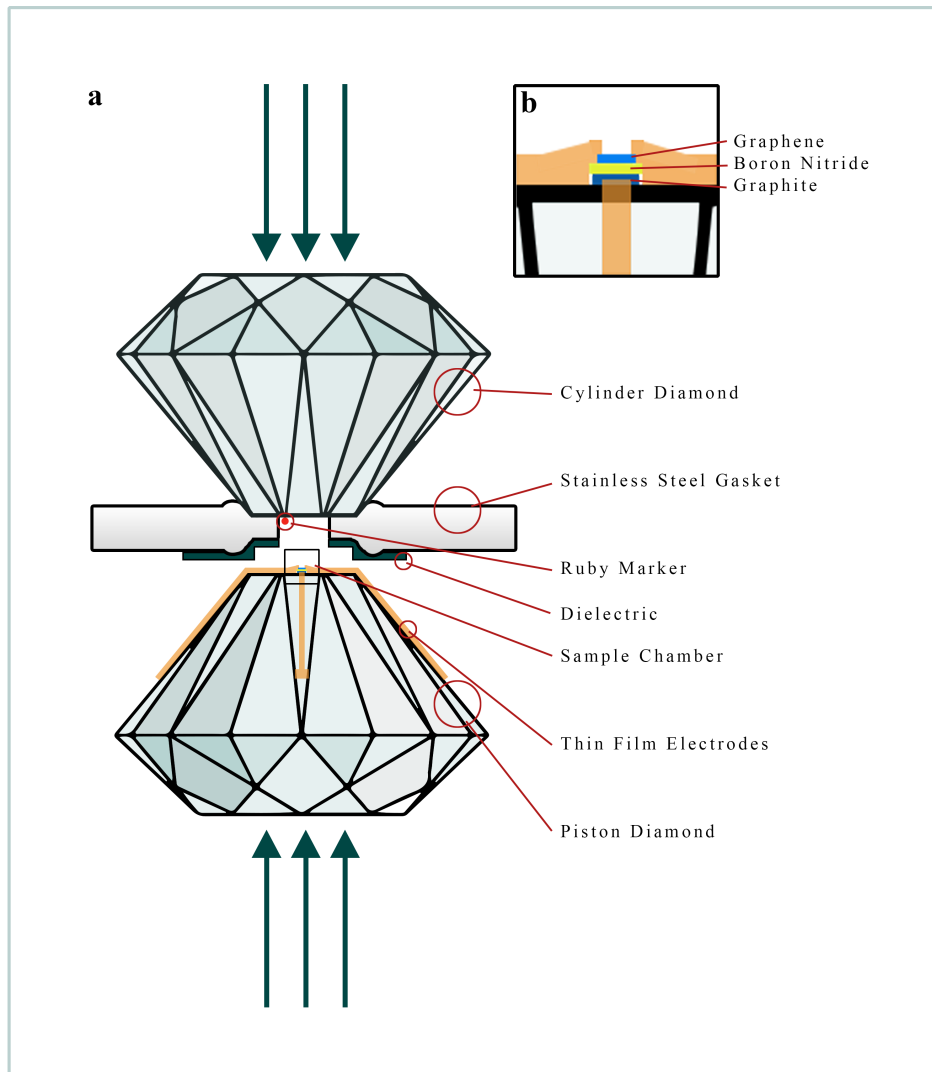
Figure 3.2: A 2D representation of a DAC. (a) Arrows highlight the direction of uni-axial compression in the pressure cell. The key identifies the materials and components of the apparatus. The stainless steel gasket is drilled-out to a desired diameter, insulated, and fixed to the cylinder diamond. A ruby ingot may be used as a pressure marker by placing it inside the gasket vacancy [6]. The sample chamber is created when the piston diamond encloses into the dielectric gasket creating a seal away from the outside environment. The piston features conductive leads in the form of thin metal films on its surface. The lead traces run from the culet of the diamond down facets of the pavilion and terminate at square pads to make connection to downstream electronics. (b) Provides a visual representation of the sample chamber highlighting the materials that create the vdW device. At the surface of the stack is graphene, followed by a dielectric of hexagonal boron nitride (hBN), and on the bottom is a graphite gate. A three terminal connection may be made to the sample by placing one electrical connection to the graphite gate and two leads across an overlapping, orthogonally-gated area of graphene.

which applies a downward force. The backing plate may be manipulated along two degrees of freedom that form a horizontal plane until the center of the diamond is aligned with the center of the backing plate. The backing plate itself is drilled out through its center to allow for various spectroscopic and microscopic techniques that may be employed through the diamond media itself. Once the closest position of center has been assumed for both diamond and backing plate assemblies, the diamonds are set and cured to the seats using Loctite™ Stycast 2850 and Loctite™ Catalyst 9.

Thereafter, the diamond/backing plate assemblies are individually placed on a proprietary apparatus to obtain a rotated angular orientation which yields the most accurate perpendicularity to axial compression. This is found by converging two reflected beams of light that generate at the table and culet interfaces of the diamond. Once found, one diamond is directly seated in that orientation to a corresponding half of the DAC, while the other is mirrored from the observed perpendicular position by 180 degrees to the other. This process ensures that as the diamonds are brought into proximity, the opposing culets form a nearly parallel floor and ceiling for the sample chamber. Interferometry may be performed when the two culets are near enough to one another to display the interference of diffuse white light between their faces when imaged through a microscope. In practice, a "good" alignment may be recognized when there are less than four or five bands of interference observed, as seen in Figure 3.3. A proper alignment is a necessary precaution to take as the diamonds themselves are considered most robust when subjected to compression in the direction of their crystallographic growth because they may crack, or break, when subjected to sufficient shearing stresses.

3.1.2   Dielectric Gaskets

A gasket with a hollowed-out chamber must be placed between the two opposing diamonds of the DAC. The gasket provides much to the instrument's utility as it offers the diamonds structural stability at the gasket's peripheral walls, and it facilitates the medium
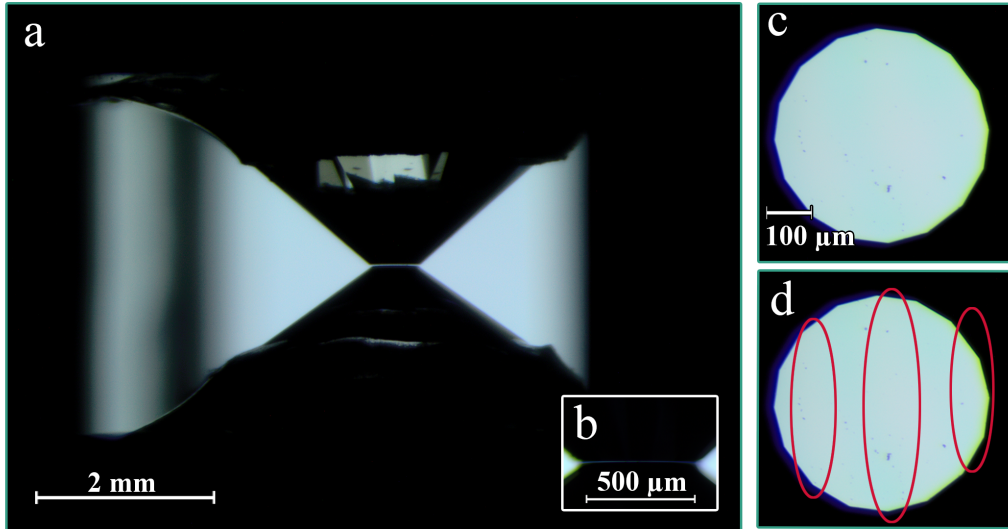
Figure 3.3: Visual indication of light interference on a diamond culet. (a) Displays a wide field of view of the diamonds in the DAC in a position perpendicular to axial compression. The backlit hairline of light illustrates the proximity the diamonds must obtain to observe the interference of scattered light between their culet surfaces. (b) A zoomed-in view of (a). Identical images are seen at (c) and (d); however, (d) provides a visual cue to the subtlety, location, and approximate geometry of the pink interference pattern that may be seen in (c). The wide banding of the interferometry indicates near parallel planes of the diamonds surface.

for the diamonds to compress into and seal the sample in an isolated environment. Gaskets in DACs are typically metallic in composition, which inherently holds benefits and caveats alike. We employ a gasket made of stainless steel, which displays characteristics of strength and ductility upon compression. Surely, hollowed stainless steel commonly makes a useful gasket for high pressure studies involving optical probes along the compression axis; however, when electrical measurements in the pressure cell are of interest, a generic stainless steel gasket must be modified in order to severely limit/impede its ability to conduct electricity. The difficulty in doing so remains at the diamond to gasket interface which is composed of sharp angles and a requirement to seal the chamber away from the outside environment at ambient conditions.

A metal sheet of stainless steel may be punched to obtain a gasket of desired diameter. After punching, the gasket is flattened in a hydraulic press and its thickness measured using a vernier caliper. With initial thickness of approximately 300 μm, the gasket is situated on top of the cylinder diamond for the process of a pre-indentation. Pre-indentation into the gasket is performed by assembling the DAC after the diamonds are seated by tightening the outer screws in a star pattern in order provide evenly distributed compression to the gasket and reduce its thickness between the points of contact. Upon observation during compression, interference patterns appear and disappear between the diamond and gasket interface at points near and after the process of enclosure. Using Raman spectroscopy, one may measure the diamond phonon peak at ambient conditions near 1332 cm^{-1} and observe its evolution to obtain a coarse measurement of the applied pressure at the culets during gasket thickness reduction [39]. At approximately 10 GPa, the DAC may be decompressed slowly as to not supply sufficient shear stress from the retaining walls to the diamonds; breakage and cracking to be avoided. Thereafter, the indentation in the stainless steel gasket may be drilled out using a proprietary laser driller. The diameter of the hole that is formed may be set by the user and should be of sufficient size to not interfere with the sample, but small enough to maintain the gasket's integrity and avoid

the potential to, 'blow-out.' Blow-out occurs when the pressure transmitting medium is able to push past the edge of culet-pavilion interface, thereby sufficiently breaking the seal between the diamond and gasket and is possible in hydrostatic or non-hydrostatic compression environments. An empirical metric is to drill out the gasket's hole diameter such that it remains in the range of one-half to two-thirds the culets' diameter.

Various methods have been employed by different researchers to insulate the hollowed gasket [40]; however, a common technique currently employed by groups in the high pressure community that study the properties of bulk materials in extreme conditions is to fill the sample chamber and pre-indentation with a mixture of powdered alumina, or boron nitride, and epoxy. This creates a dielectric medium for the diamond to squeeze into. The process is quite coarse and may lack the precision needed for 2D samples due to their fragility. The bulk technique, common to high pressure studies, may require the DAC to undergo multiple pre-compressions into the dielectric to pelletize the insulting powder throughout the chamber, which could limit the potential for the dielectric powder to flow inward under compression. The remaining portion of the circular gasket is insulated using transparent tape and quick-set epoxy at the interface of tape and alumina. Bearing in mind that the diamond will at one point have superficial electrodes on its exterior, maintaining a proper gasket that can conform to both the pressure and electrical requirements is of utmost importance. The delicate process of exfoliating and stacking atomically thin heterostructures is to come, and the methods in which the gasket are insulated, may be problematic in conjunction with one another if not investigated further. It is possible to use a variety of different media on the gasket, and Forestier et al., has performed tests on 2D materials in a DAC using parrafin oil, or a 4:1 mixture of methanol-ethanol [34].

In this study, the aforementioned bulk technique using alumina and epoxy as the method of insulation was performed on two different DAC systems with both success and failure, as discussed in Chapter 4. Furthermore, it should be noted that there may be a way to insulate the conductive stainless steel gaskets using atomic layer deposition (ALD)

by growing thin layers of alumina on the gasket itself, or, through other methods, such as utilizing the spin-ability of the Merck™ AZ4110 photoresist to hard-cure a permanent dielectric to the surface of the gasket. Surely, the solution to creating a functional dielectric for 2D materials in a DAC is close to fruition.

3.2 Nanofabrication of Carbon-Based van der Waals Heterostructures

To understand the characteristics and requirements for nanodevice fabrication, we must first come to conceive the methodology needed to obtain and isolate atomically thin 2D samples, pick-up, stack, and transfer them to a diamond anvil substrate. Nanofabrication is a process by which electrical devices are made with materials having dimensions in the nanometer (10^{-9} nm) range. The methods of this process have been used in, developed by, and applied to various fields such as nanophysics, 2D physics, nanotechnology, electronics, photonics, and computing. In general, research on vdW heterostructures investigates the interactions between heterogeneous materials that are layered atop of one another and the layers are held together by the van der Waals force.

3.2.1 The Process of Exfoliation & Selection

Exfoliation is the technique by which samples, or flakes, of the targeted materials are removed from their bulk crystal and isolated on a preliminary substrate. The substrate is scanned for ideal specimens/flakes under a microscope. Four-inch wafers of silicon may be used as an excellent substrate for exfoliation due to its optical properties under white light illumination. The wafers themselves are composed of 500 μm thick high-purity silicon at its base and topped with a 300 μm thick layer of silicon dioxide (SiO_2). The SiO_2 layer adds an extra transparent medium for the optical imaging of the flakes [3]. The wafers may be diced to an appropriate area of approximately 1 cm^2 using a diamond scribe to create
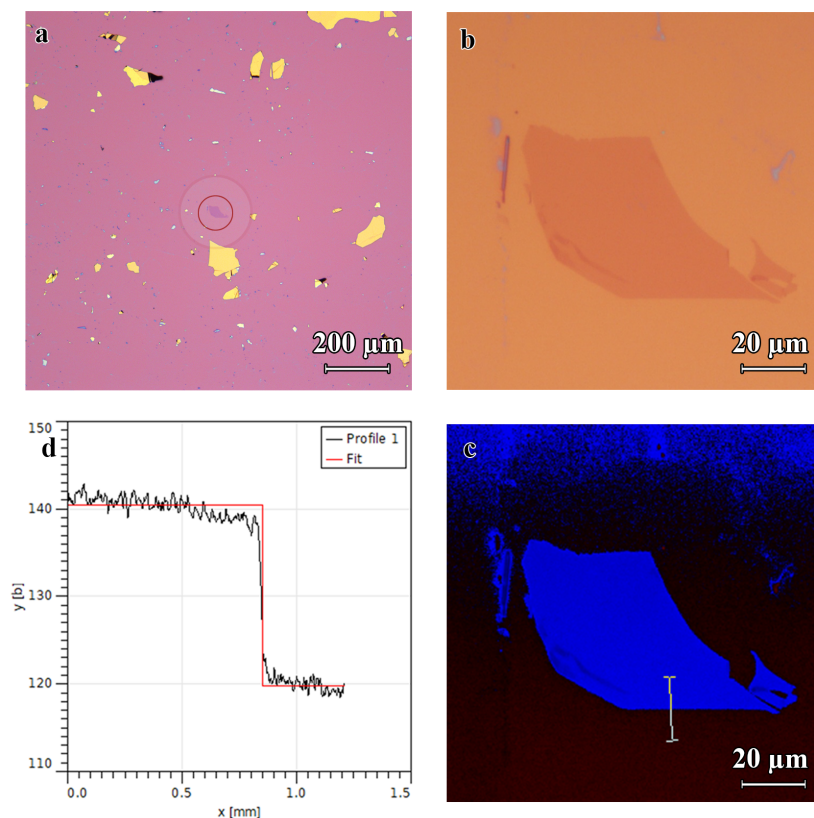
Figure 3.4: Microscopy of the products of exfoliation. (a) Displays a 10x magnification image of flake of trilayer graphene on an SiO_2 substrate. The flake has been highlighted with a red circle to indicate its location. (b) Displays an image of the same trilayer flake at 100x magnification. The image shows a fairly homogeneous thickness across the flake, represented by an even hue. (c) Displays the same image from (b) processed through the green channel of the digital image spectrum. A line cut may be seen on the image itself that passes along a near perpendicular path from the flake to the substrate. The reflected contrast profile may be analysed using the signal shown in (d) in Gwyddion whereby the high-signal corresponds to the flake and the low-signal corresponds to the substrate. The ratio of the two signals provides a value that may be used to quantify the n×layers of the graphite flake up to 3-4 layers of graphene.

square-like chips. Thereafter the individual chips must be cleaned through sonication in a submersion of organic solvent environments. Once the chips have been cleaned using acetone and isopropanol, they are dried on a hot plate as molecular N_2 gas passes over them. The cleaning process is incredibly important as it is the first step in obtaining useful and clean materials for study - if care is not taken during the cleaning process, it is possible for potentially good flakes to become compromised through dirt, dust, and other microscopic particles. For these reasons, all chips are also kept in a desiccator, or glove box, to reduce the available water, or oxygen, in the environment surrounding the chips.

In general, flakes are exfoliated from the bulk material using a technique that involves Scotch™ tape [3]. To obtain samples of graphene, we coat a small area on a strip of tape (approximately $1\,mm \times 10\,mm$) with bulk samples of graphenium (NGS Trading Consulting GmbH, www.graphit.de). From the backside of the tape, the pressure of one's finger is enough to create the aforementioned coating and impress enough material on the tape's adhesive side with an abundance of graphite. Thereafter, the first coating is exfoliated to the rest of the tape by placing every possible part of the tape's adhesive back onto the original coating of graphite. Visually, it looks as though the tape began with a small strip of graphite flakes on the adhesive side, and eventually the graphitic flakes completely cover the strip's adhesive side. At this point, we have created a master strip called, "The Parent Tape." Somewhere within the exfoliated layers of the parent tape there is a flake of graphene that is to be isolated and studied. Isolation of the sample is also a two-fold process as cleaving the layers of graphite from the parent tape is performed using a similar piece of virgin tape, "The Daughter Tape." The daughter tape is overlaid entirely on the parent tape, creating a mirror-like image of the samples therein. Upon pulling the two strips of tape apart, the daughter tape further cleaves away layers of the existing graphite from itself and ultimately exposes at its surface more interior layers of the graphitic system.

The previously diced and cleaned silicon chips are then oriented with the SiO_2 facing

upwards. The adhesive side of the daughter tape is overlaid on the chips and contact between the layers is smoothed out using a straight edge and modest downward pressure. Pulling the tape away from the chips is a two-handed process as the adhesive will simply keep hold of the chips unless remedied by an external grip. Slowly, the tape is pulled away from the chips and the samples that are left behind on the silicon substrate were transferred through van der Waals forces. Figure 3.4 shows the potential yield from the final step of exfoliation as well as displays the isolation of atomically thin samples whose layer number can be characterized using microscopy and contrast analysis.

Scanning each individual chip at 10x magnification allows for the potential to recognize useful samples due to their color profile[3]. In Figure 3.4, (a) and (b) display an isolated sample of monolayer graphene on a silicon substrate imaged with both a 10x and 100x microscope objective. It is possible to identify samples of greater than approximately 10 μm in radius as you move across the chip. When samples have been identified at 10x magnification they are quickly verified of their practicality at 100x magnification and are catalogued for future use.

Verification of the thickness of the exfoliated samples may be performed through open-source contrast analysis software called Gwyddion. Gwyddion can be used to process image maps and apply line profiles to specific regions [41]. The thickness of the flakes in question may be extracted by taking line cuts through the flake and substrate within a singular channel of an RGB color spectrum. We utilize the green channel as our standard channel and find that the software processing is not only consistent but of greater temporal efficiency when compared to other methods for device characterization, such as, observation of the 'C' peak in Raman spectroscopy. The output from the measurement provides the user with an intensity profile of the reflected light from the substrate and through the sample. The difference in the intensity, as seen in Figure 3.4 (c)-(d), shows a relatively perpendicular contrast profile between the flake and substrate and allows for a calculation of the contrast ratio. This contrast ratio is seemingly arbitrary, but remains
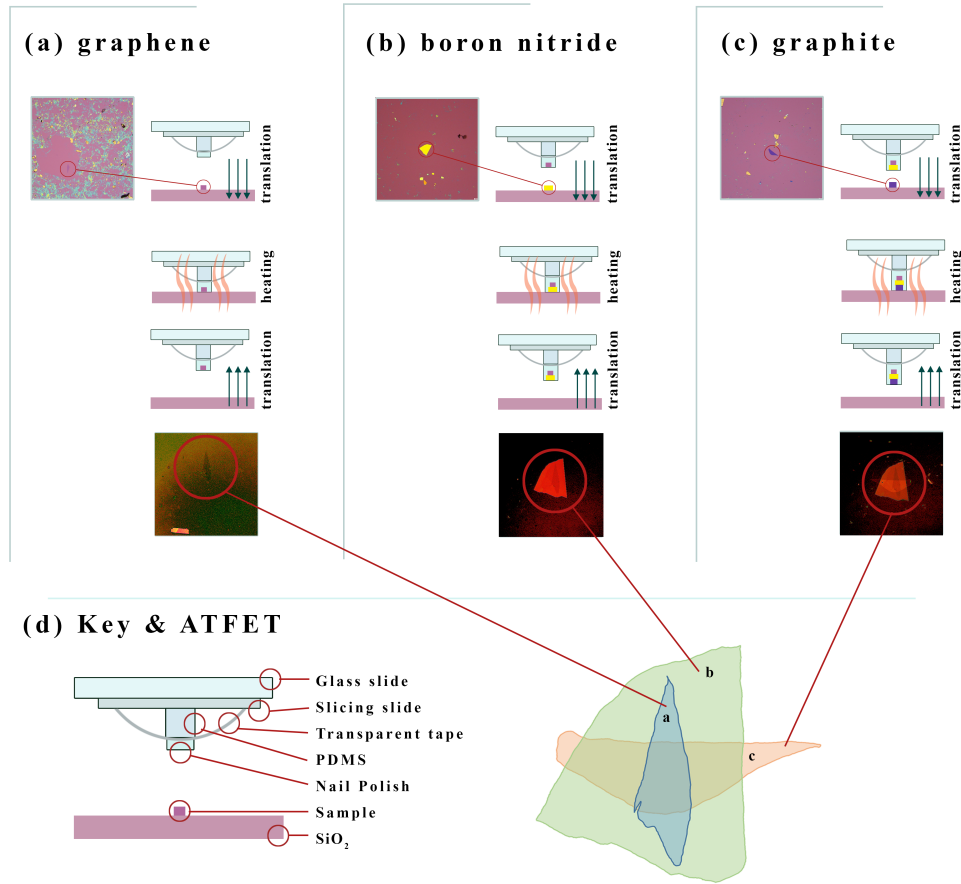
Figure 3.5: Applied methodology to pick up 2D materials. The vdW heterostructure is composed of atomically thin flakes which stack atop of one another to form an atomically thin field effect transistor (ATFET). (a) The 10x image on the left indicates the location of the first target flake. Directly to the right, a 2D representation shows the progression of picking up a target flake with common nail polish. The transparent media on a glass slide, shown in (d), is translated downward as a whole toward the SiO_2 substrate and heated on a stage until the polish laminates over the flake. Lamination reaches a steady state temperature of 70 °C and is set to cool. At a steady state of 40 °C, the slide may be translated upward, lifting the flake from the SiO_2 substrate. The final image of (a) is an enhanced image at 20x magnification that corresponds to the BLG flake on nail polish. (b) A 10x magnification image of a flake of hBN on a SiO_2 substrate and follows the same technical progression for picking up hBN using slide translation, heating near a steady state temperature of 70 °C, cooling, and physically lifting the slide to remove the flake from the substrate via translation. The last image of (b) displays an enhanced image at 20x magnification of the corresponding hBN and BLG flakes on nail polish. (c) A 10x magnification image of a graphite flake on a SiO_2 substrate and follows the same technical progression for picking up graphite as the other flakes mentioned previously. The last image of (c) displays a contrast image at 20x magnification of the corresponding graphite, hBN, and BLG flakes on nail polish. The enhanced images at the bottom of (a), (b), and (c) feature a red circle identifying and pointing to a outlined representation of the vdW heterostructure, illustrated in (d).

consistent along the flake edge when images displaying flakes of identical physical atomic thickness are processed.

3.2.2   Stacking & Transferring a van der Waals Heterostructure

All van der Waals heterostructures vary in size and shape; therefore, the methodology employed to stack the exfoliated flakes therein begins with spatial assessment and a plan. Through geometric orientation, a coarse, structural blueprint may be curated to guide the eye during the pick-up process. All pick-ups are performed under micromanipulation using a glass slide retrofitted with a few optically transparent aids and common nail polish [42], as depicted in Figure 3.5 (d). The position of the silicon dioxide substrate and target flake is positioned near, but not directly below, the touch down point of the inverted nail-polish slide. As the nail polish and and substrate come into contact, an evacuated stage holding the chip in place is heated to promote flow of the nail polish over the targeted flake. As the nail polish heats up, it becomes less viscous and laminates over the target flake. Finesse touch allows for the heated stage to continue an increase in temperature without significant growth of the contact area. When the nail polish and substrate achieve a steady temperature state, the heated stage may be turned off allowing the polish to cool and harden over the flake and entire contact area.

When the temperature ramp falls back to ambient, the z-stage of the slide manipulator may be actuated in order to slowly lift the flake from the silicon dioxide. Doing so typically allows for a complete pick up of all flakes interior to the contact area. This process should be repeated for each targeted flake of the stack until the desired heterostructure has been removed from the substrate and assembled on the polish. In Figure 3.5, the final image in (c) displays a nail polish slide with a vdW heterostructure inverted on its surface - ready for transfer to a diamond anvil substrate after the slicing slide has been removed and placed in the DAC transfer jig, as seen in Figure 3.6.

Figure 3.7, shows the temperature ramps that achieved success after each stacking
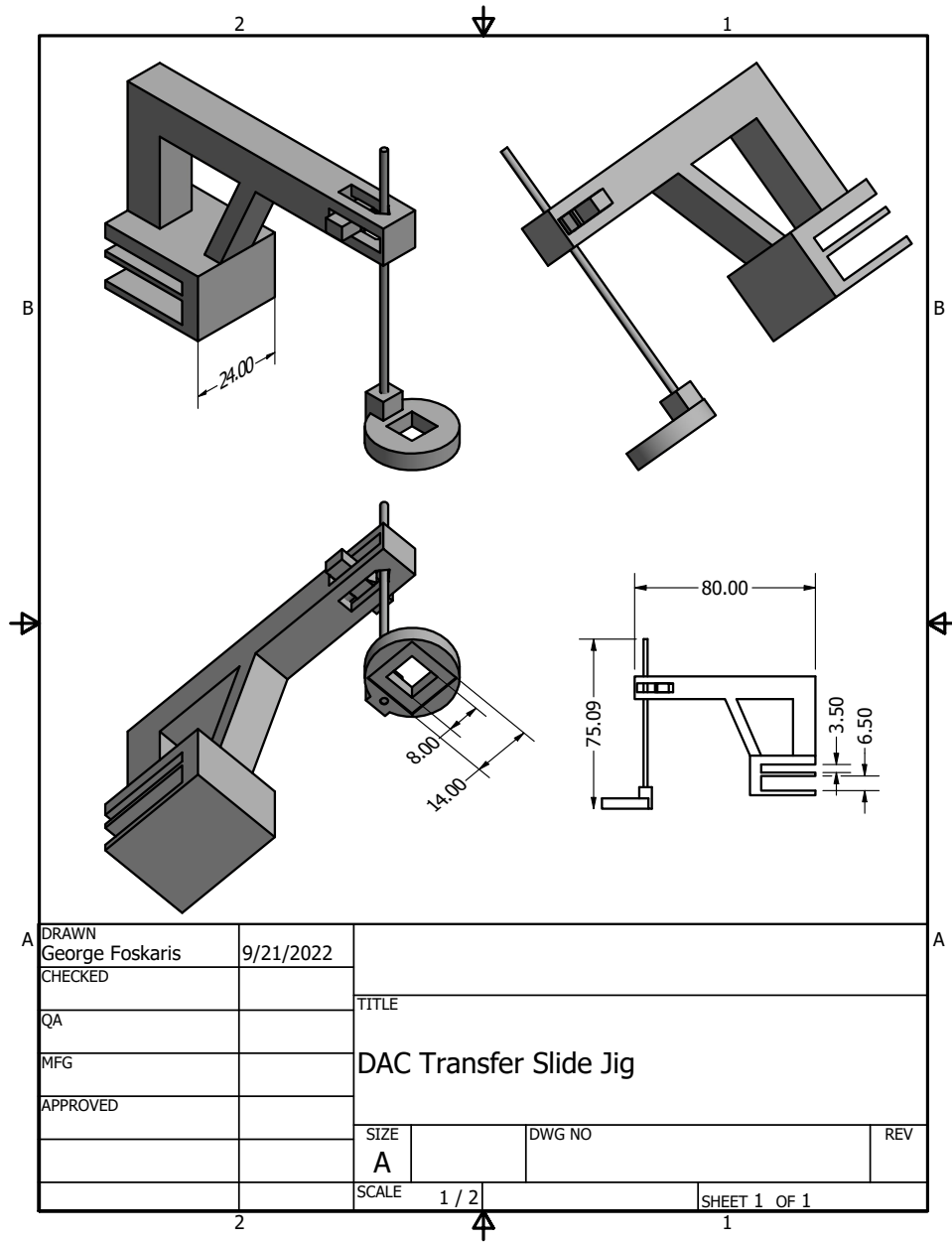
Figure 3.6: The DAC transfer-slide jig was designed to accommodate the transfer of the ATFET given the geometry of the PEAS DAC. The retaining walls of the PEAS DAC are spatially extensive such that they are greater in height than the tip of the diamond's culet when the piston is laid flat on its outer chassis. The jig is designed to fit into the micro-manipulator assembly that carries glass slides of 1mm, the DAC transfer slide jig utilizes a center pole and viewing window for transfers under microscopic supervision. The tape holding the slicing slide, seen in (d) of Figure 3.5, may be cut while the glass slide beneath it is removed. It is then taped to the surface at the bottom of the pole and viewing window on the jig, as seen in the bottom left illustration. Transfers occur when the nail polish has been melted to the diamond anvil substrate. Dimensions of the design are listed in millimeters.
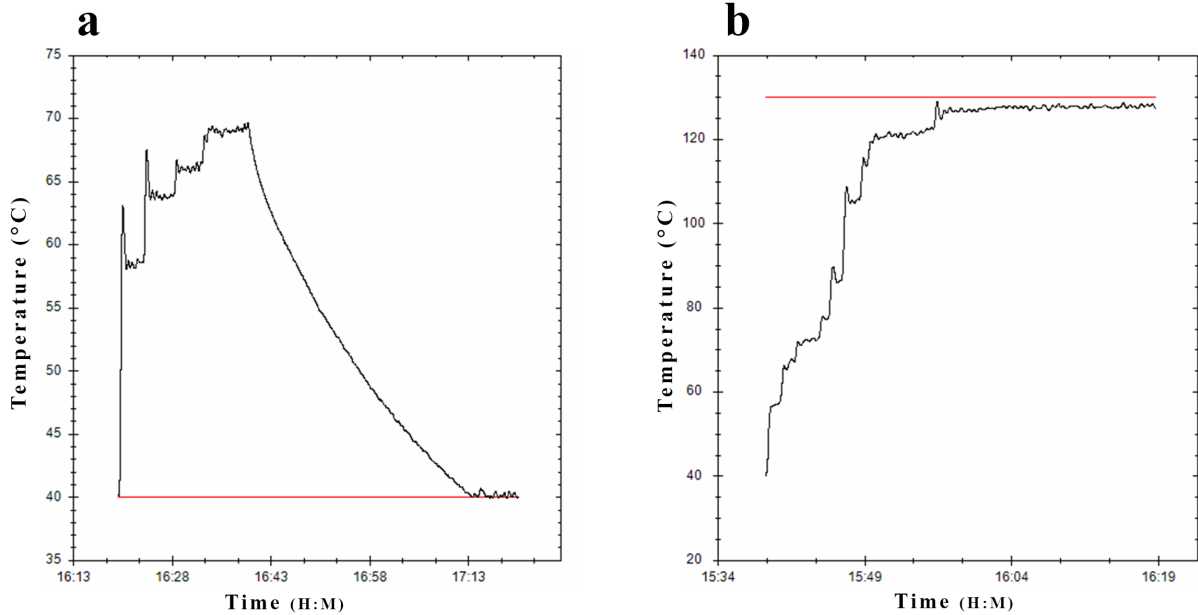
Figure 3.7: Picking up and transferring vdW heterostructures using a heated stage. (a) Displays the temperature ramp used for picking up 2D materials with common nail polish. The mechanical methods of which are depicted and described in Figure 3.5. The heated stage can be increased in intervals of 5 °C - 10 °C until the target temperature has reached a steady state and laminated over the target flake(s). Thereafter, the stage is left to cool until it reaches a steady state at set point temperature of 40 °C. Thereafter, mechanical translation of the pickup slide will lift the flake from the substrate. Once the vdW heterostructure is assembled on a nail polish slide, the slicing slide is removed from the glass slide and taped into place on the transfer jig, as seen in Figure 3.6. (b) Displays the temperature ramp used for transferring a stacked vdW heterostructure to a diamond anvil culet. The mechanical methods are similar to those of pick-ups whereby they utilize a translation stage to bring the stack in contact with the culet. Upon contact, the temperature ramp is set to 130 °C in 5 °C - 10 °C intervals until the polish is in a viscous melt. The jig is then translated away from the substrate until a string of the melted polish separates from the transferred stack and the jig assembly. This may be visually seen in Figure 3.8.
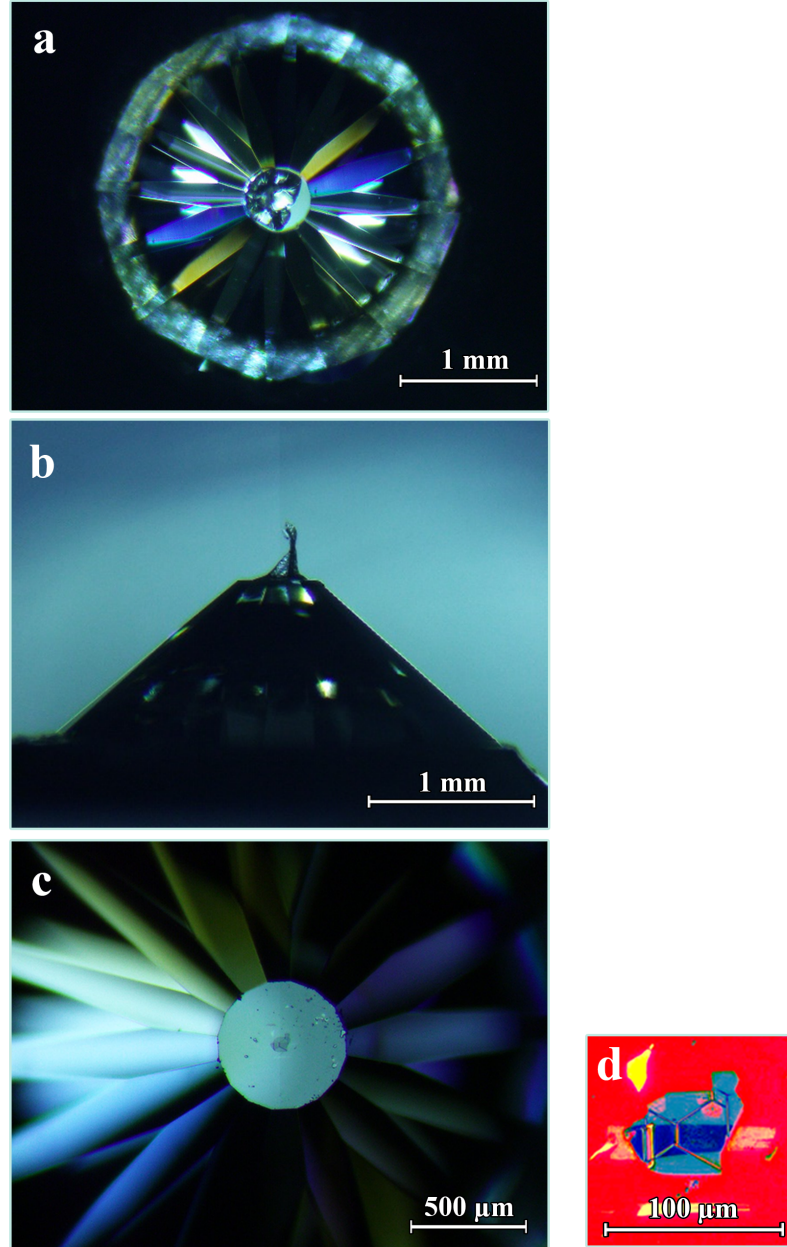
Figure 3.8: Images depicting visual quality of melted nail polish on a diamond anvil. (a) Displays the top of the diamond anvil immediately after stack transfer with nail polish on the surface of its culet. (b) A side profile of the same physical quality seen in (a). (c) An image displaying the vdW heterostructure near the center of the culet. (d) A zoomed-in view of the vdW heterostructure with an enhanced color profile to emphasize the layers of the stack.

iteration as well as the temperature at which vdW heterostructures may be transferred to a diamond anvil culet. A visual example may be seen in 3.8, where (a) and (b) display the physical appearance of a melted polish to the diamond anvil substrate from perpendicular perspectives. In Figure 3.8, (c) displays the diamond anvil after the nail polish has been dissolved in an acetone bath revealing the vdW heterostructure on the culet. Figure 3.8 (d) features a zoomed-in view of the flake that has been enhanced to highlight the different layers of the vdW heterostructure.

Once the vdW heterostructures has been transferred, the culet of the diamond may be photographed at 10x magnification (or any magnification that corresponds to the objective of the instrumentation used to perform photolithography at the desired resolution) to provide a base image during the creation of a 2D computer aided design (CAD). The 2D CAD should feature an electrode pattern that can be uploaded and implemented as a digital mask in the maskless photolithography system. Figure 3.9 illustrates different designer masks that feature different characteristics, such as potentials for lead redundancy and illumination area. Depending on the region of the heterostructure that is to be gated, it may be necessary to create a pathway for electrical connection within 10 microns of precision. Using an microscope objective with 10x magnification our photolithography system consistently allows for resolved development of 3 microns at the electrode-tips. The ability to resolve structures at this level of precision is crucial in the study of 2D materials as the samples in study are often times as small as tens of microns in length (or width).

3.3   Photolithography

3.3.1   Masks and Photosensitive Polymers

Transforming a diamond anvil substrate into an electronic device may be realized by first performing photolithography on diamond. The metrics of which were tested and determined, and may be seen in Appendix A. Photolithography is the process by which a
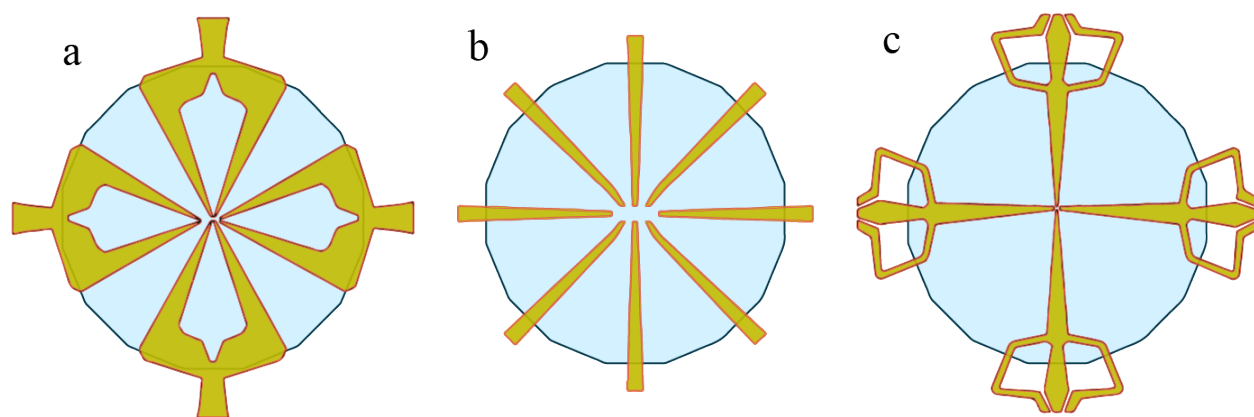
Figure 3.9: The three panels display different electrode pattern designs that were tested as masks for photolithography. (a) Displays a four probe electrode pattern with a double redundancy at the electrode tips. The design was tested on modified brilliant cut diamonds and was proven to be unusable due to large exposure area of the pattern near the edges of the culet which contribute to internal reflections that propagate through the crystal and cause unwanted areas of overexposure. (b) Displays an eight probe pattern on the diamond anvil that yielded positive results and was tested on an initial sample of MnS_2, discussed in Chapter 4. (c) Displays the electrode pattern used on the gtf005 device, discussed in Chapter 4, and utilizes thin electrodes with redundancies over three edges of the culet-pavilion interface in order to create more contact traces to the electrode tips in the event of potential shearing of the leads with the gasket upon compression.

photosensitive polymer is exposed through a designer mask in order to develop an image that is focused onto the surface of some base material [43]. There are two types of photosensitive polymers, called photoresists, that produce different results during development. The results correspond to, 'positive,' or, 'negative,' designs. A positive photoresist is one such that the interaction of the associated focused light with a region of the polymer breaks a saturated network of bonds of the polymer in that region, leaving the exposed image soluble in a development bath. In contrast, a negative photoresist leaves the associated exposed image insoluble when subjected to a development bath. This research solely employs positive photoresists.

Electrical lead positives may be exposed throughout the pavilion and culet of the diamond substrate, but the entire piston must be processed as a whole unit as to not break alignment with the opposing diamond of the cylinder (or vice versa). This constraint offers a difficulty in physical processing because the act of photolithography includes many steps; the overview of which may be summarized and listed as: photoresist spun to the substrate, hardening of the photoresist through a baking/curing process, image/design exposure through a mask, multiple submersions of the substrate into different chemical baths, deposition of thin-metal films, and liftoff (the process of removing unwanted material from the substrate). To perform these steps and maintain alignment, various tools were required for fabrication and testing. Some of the tools became essential, and the others were deemed useful, but superfluous. Figure 3.10 displays the blueprint for an original chuck assembly that was designed to brace, and temporarily lock, the entire DAC piston in order to maintain concentricity and promote an even-coating during the spinning of photoresist. The chuck was designed to seat directly to spindle of the spinner in the cleanroom of the Science and Engineering Building at the University of Nevada, Las Vegas. The DAC chuck design proved essential and critical for the coating of photoresist as without it, the DAC geometry and mass will generate sufficient torque when spun to rotate/fling off the spindle.
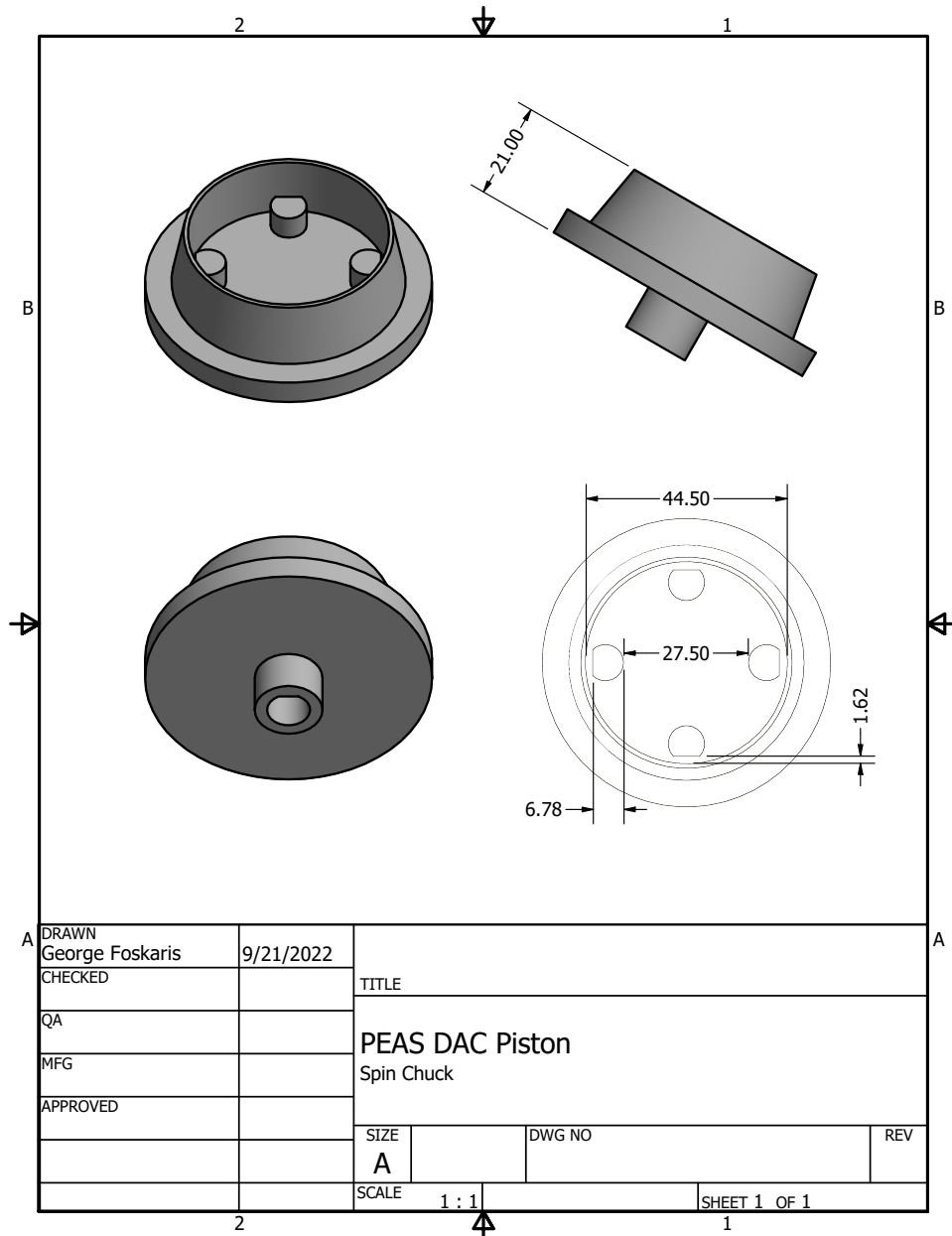
Figure 3.10: The PEAS DAC-piston chuck was created to spin LOR and photoresist to the diamond anvil substrate. It allows the PEAS DAC piston to sit inside the walls of the retaining chuck and lock in place via four plugs that are found on its base. The plugs fit inside the set-screw holes on the outer piston chassis and the process locks the piston in place to ensure that the the DAC is able to spin near its concentric center at thousands of RPM, promoting an even and homogeneous coating during the spinning process. Every iteration of photolithography performed on the PEAS DAC piston utilized the chuck as it proved to be essential for safety, as well as for producing the photosensitive base coat to the diamond anvil for photolithography. Dimensions of the design are listed in millimeters.

3.3.2 A Bilayer Recipe of Photoresist

To ensure good liftoff of the resist and unwanted conductive metals, proper processing requires a bilayer recipe of photosensitive polymers. The bilayer recipe is helpful because the angular geometry of the diamond promotes an uneven distribution of the liftoff resist (LOR) and photoresist which ultimately creates a difficulty when isolating the electrode tips and electrode leads over the interface between the culet and the pavilion of the diamond. Using an initial coating of Merck™ LOR, the DAC piston may be spun at 1000 RPM to obtain approximately 1 μm of an LOR thickness coating on its culet surface. It is then baked at 150 $°C$ for 20 minutes and allowed to cool. Thereafter, the DAC piston is placed back in the chuck assembly and spun with Merck™ AZ4110 photoresist at 2000 RPM to obtain an approximate 2 μm thick coating of photoresist at its culet surface. The full assembly of the DAC piston is baked on a hot plate again at 95 $°C$ for 15 minutes and allowed to cool to room temperature. The layer of LOR has a faster development rate when subjected to the same exposure as the resist which produces an undercut in the polymer which is visible under microscope. The undercut will later allow for solvent fluids to rush into vacancies underneath the coating of the superficial photoresist. Furthermore, the use of a hotplate to bake the DAC piston assembly as a whole is recommended as better results were consistently obtained when curing through thermal conduction of the substrate, i.e. curing from the inside-out of the DAC piston as opposed to through thermal convection which cures from the outside in. It should be mentioned that these metrics for proper adhesion and curing of the LOR and photoresist differ from standard procedure on a silicon dioxide substrate.

3.3.3 Developing an Image on a Diamond

The photo-sensitivity of the photoresist lies in the blue region of visible light; therefore we use a photolithography system of fixed wavelength centered about 413 nm to ensure proper reaction and exposure of the photosensitive polymers through the electrode
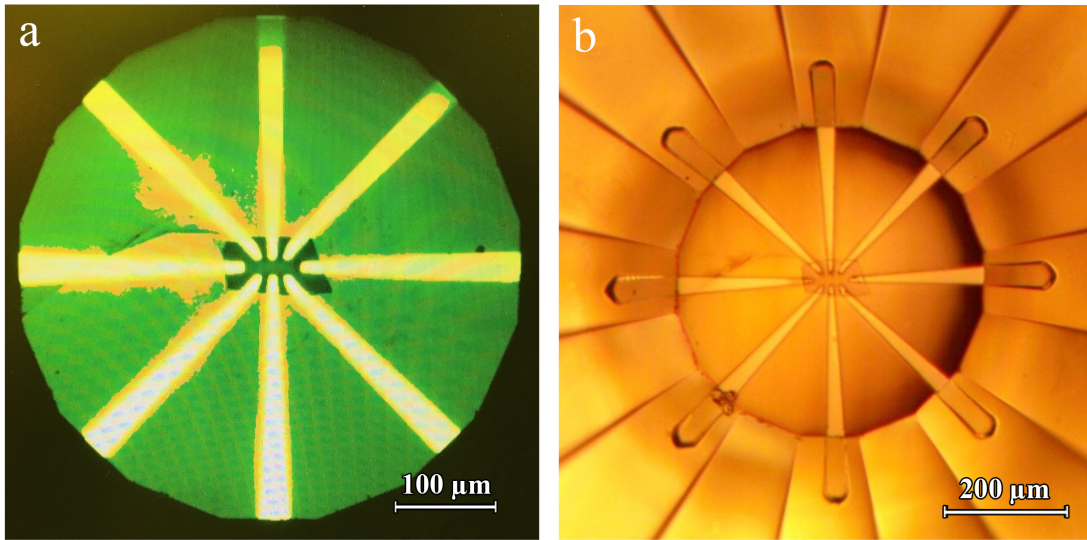
Figure 3.11: Images of photolithography on diamond. (a) Displays the process of alignment and exposure during photolithography. The eight leads that make connection to the sample at the culet's center are exposed through the digital mask. (b) Displays the electrode channels that have been revealed to the sample on the diamond substrate upon development. The quality and resolution of the photolithography is dependent on the cut of diamond used. Both (a) and (b) were performed on a standard cut diamond. The finest resolution at the electrode tips is 3 μm. It should be mentioned that the areas of the diamond that do not correspond to the electrode patterns still have LOR and photoresist on them.

mask. Upon exposure, the polymer network of the photoresist is broken and left susceptible to dissolution in a development bath. Figure 3.11 (a) shows the process of alignment on the maskless photolithography system as well as the developed positive on the diamond anvil substrate in Figure 3.11 (b).

When electromagnetic radiation (EMR) propagates between media there is a reflection at every interface. Although diamonds are optically transparent to a large region of electromagnetic radiation, they reflect EMR off of their outer and inner boundaries. The light that transmits through the diamond is slowed, refracted and eventually meets another boundary. These properties, although hastily summarized present challenges when

performing photolithography on diamond. The amount of light that is able to interact with the photoresist must be minimized in order to create well resolved positives. If too much light is propagates through the crystal, there will be over-exposures found along the edges of the diamond. Given the physical size of the diamonds and the spatial attributes of the digital masks the angles of incidence of the EMR may present challenges if not accounted for and issues with over-development were commonly observed and remedied, whenever possible.

3.4   Electron Beam Deposition

Once the image positive has been developed out of the resist revealing the diamond substrate, thin metal electrodes may be deposited directly to the diamond anvil using electron beam deposition (EBD). The DAC piston is placed in an retainer which may be suspended in a rotating carousel of the EBD chamber. An original design was developed to create such a retainer and can be seen in Figure 3.12. By applying a high-voltage to an anode at a specified current and chamber pressure, EBD methodology allows for the ablation and deposition of a target metal to a substrate at an optimal interval, or deposition rate. The desired metal is the cathode of the system and is positioned in a crucible on a turret in the chamber.

The metal growth obtained on the substrate may be of a desired thickness by measuring the mass density of a calibrated quartz crystal found in the chamber. The film deposition obtained is isotropic and highly oriented on the substrate. The process forms the microscopic connection to the samples in question. We use a 7 kV EBD chamber and apply currents up to the range of 200 mA. The exterior electronics and turret are water cooled to keep the system from overheating during current ramping and the chamber is evacuated using a cryopump to obtain a pressure of approximately 2×10^{-8} $torr$ before power is ramped in the system and deposition is commenced.
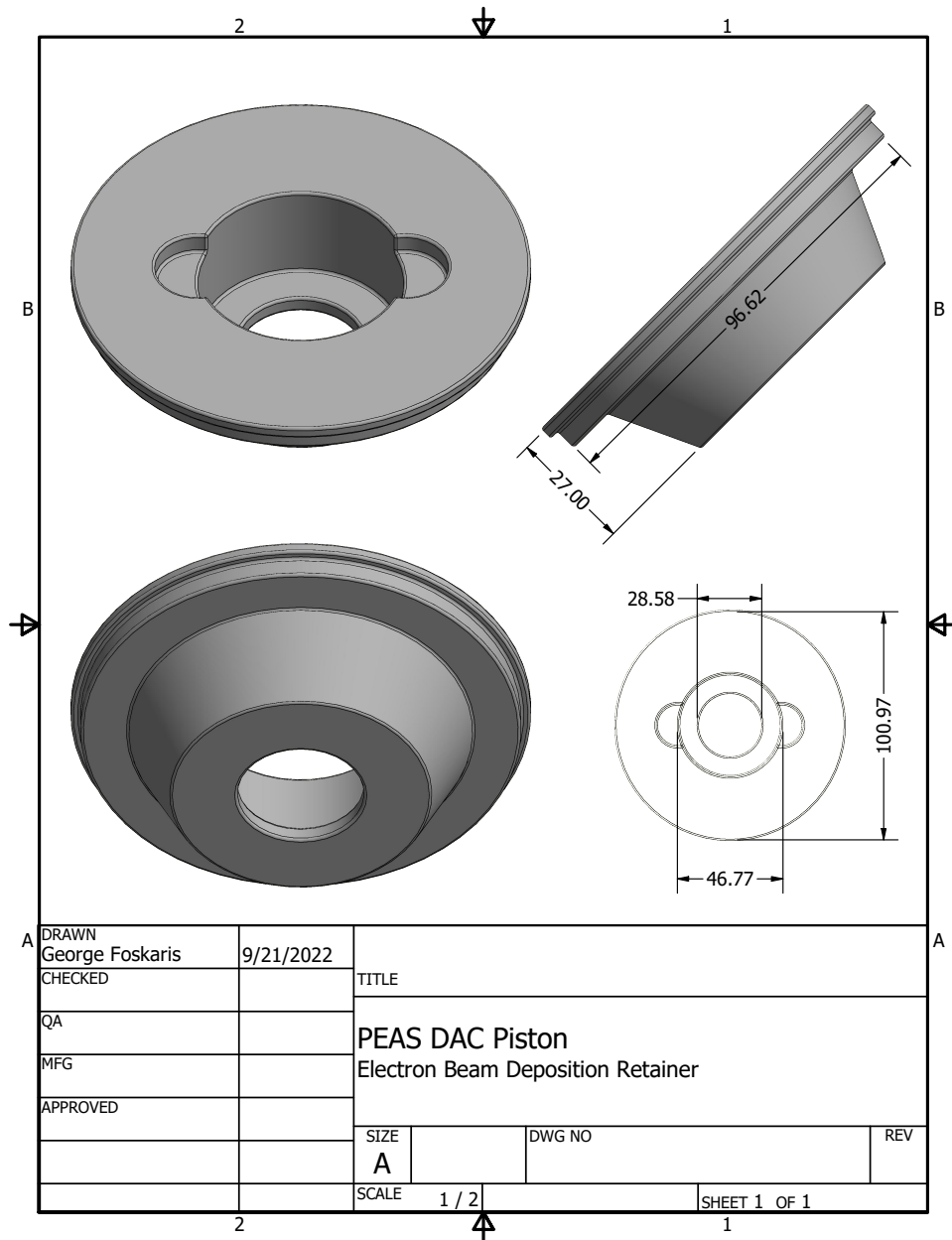
Figure 3.12: To mount the PEAS DAC piston in the carousel of the EBD chamber, the associated retainer chassis was created. The retainer, made of aluminum, allows for the DAC to be seated in a cradle and suspended in a bracket. An essential tool in the process of depositing metal films to the diamond anvil substrate as the opening at the bottom allows for ablated metals to pass through the vacuum chamber and retainer chassis making direct contact with the diamond anvil substrate. Dimensions of the design are listed in millimeters.

47
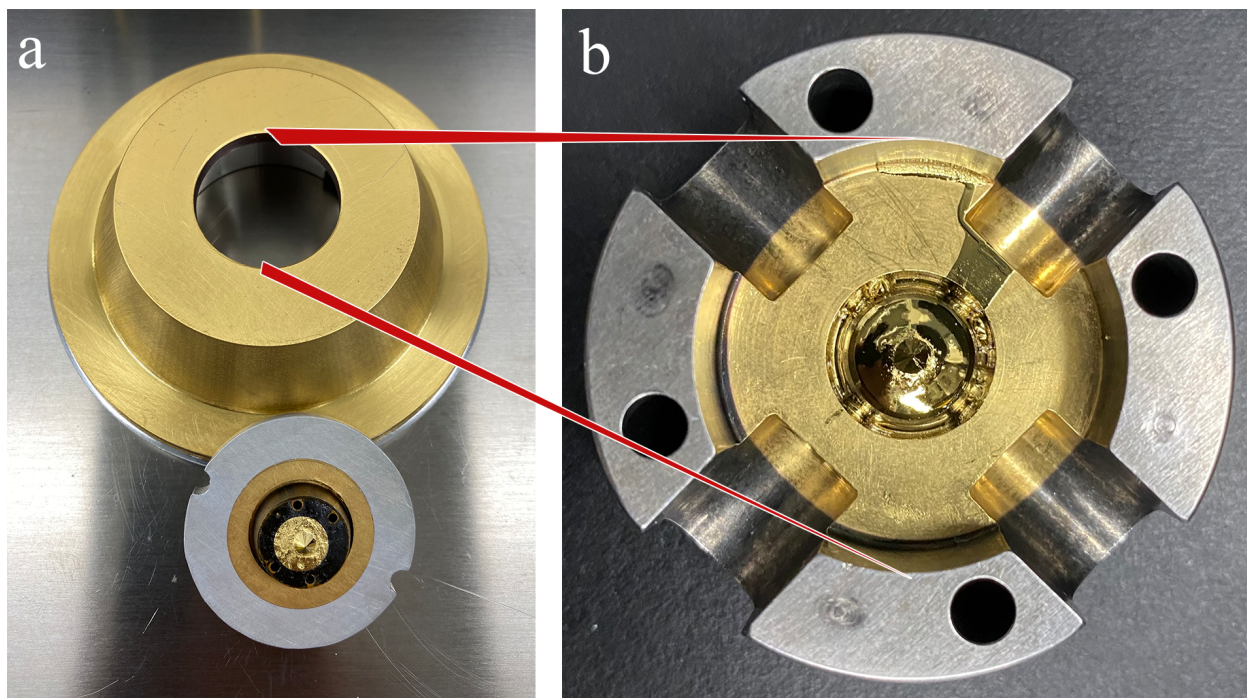
Figure 3.13: Isotropic deposition of thin-metal films. (a) Displays an image of the underside of the EBD retainer directly after deposition of chromium and gold. The object towards the bottom is a seated diamond that was used for process testing and a spatially reduced puck that was designed to hold it in the EBD retainer chassis. The red arrows that lead to panel (b) point to the relative geometric position of PEAS DAC inside the EBD retainer and the relevant circular surface area of the DAC subject to deposition. One may see that they align vertically when seated together. (b) Displays the homogeneity of the metal deposition to the surface of the diamond anvil piston. It may be helpful to observe that the base of the piston within the inner walls is fully coated in chromium and gold, including the backing plate, the retention screws, and the diamond itself.

3.4.1 Metal Selection

Once target chamber pressure is obtained, we perform an initial deposition of chromium at nearly 0.5 $\mathring{A}/s$ until we have deposited nearly 10 nm of the metal. Chromium is used as an initial layer as it is naturally abundant, economical, and has better than satisfactory electrical and mechanical properties. It is also commonly used in 2D studies to promote better adhesion with the substrate. We find an ideal deposition rate at an applied current of in the range of 30-40 mA in the EBD chamber. The final depositional coating uses gold as it makes an ideal electrode plating material due to its high conductivity and its inert characteristics. Using high-voltage EBD, gold has an optimum deposition rate near 1.0 $\mathring{A}/s$ which is found at nearly 100 mA of applied current in our system. Figure 3.13 shows a physical image of the PEAS DAC piston and the EBD retainer immediately after removal from the EBD chamber.

3.4.2 Liftoff - Isolation of the Electrodes

The removal of unwanted conductive leads is performed during the process of liftoff. To reiterate, during pre-processing, both LOR and photoresist were spun to the diamond anvil substrate and after exposure and development of the electrode pattern, the diamond substrate is superficially revealed in the target region, whereas the remaining LOR and photoresist remain on the surface of the diamond. EBD isotropically covered the entire substrate in Cr and Au films, as seen in Figure 3.13. To remove the bulk of the conductive metals, the DAC piston is submerged in a bath of Merck™ Photoresist Remover. To promote a good liftoff, the LOR allows for a higher rate of development under the photoresist, which in turn creates an "undercut," or an area where the thin film deposition is able to detach from the photoresist surface. The final product is depicted in Figure 3.14. Liftoff may take tens of minutes to complete and still may need agitation in a sonicator to break the connections between the electrode tips of the culet.

The fragility of the electrodes on the diamond substrate is paramount to recognize as
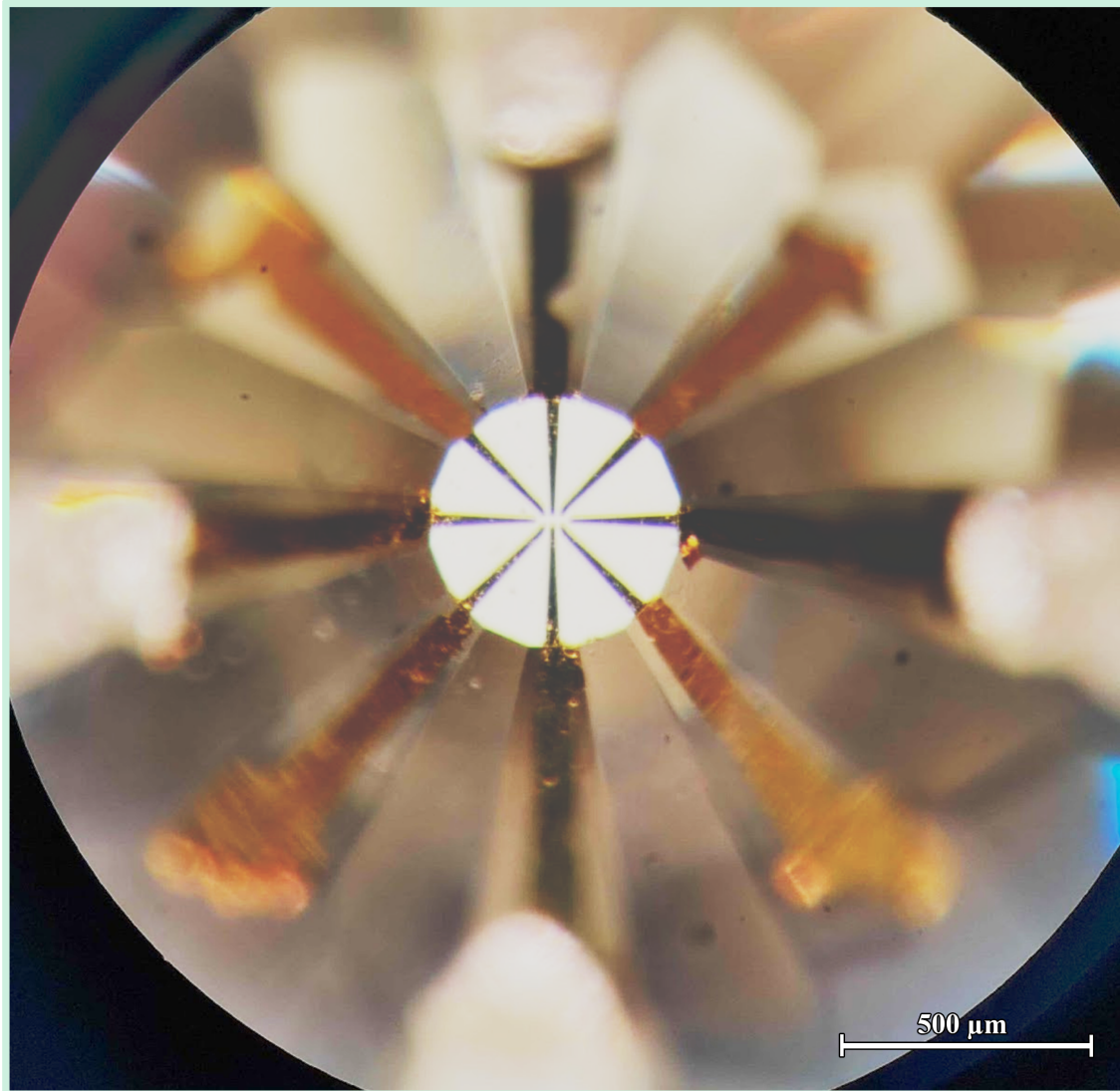
Figure 3.14: An image of the diamond substrate after liftoff. The eight probe design allows for connection to eight different electronic leads and maintains a tip resolution of 3 μm that may be made to microscopic samples. The bright center of the culet is due to the transmission of a light source through the bottom of the pressure cell. The deposition of thin metal films to the diamond verifies the functionality of photolithography, electron beam deposition and relevant development processes on a diamond substrate.

the bond between the electrodes and the surface of the diamond may be attributed to van der Waals interaction. If the substrate is left to dry without all of the unwanted metal film removed, any residual resist may harden to the surface and become increasingly difficult to dissolve. Therefore, if sonication is needed, the DAC piston should never be allowed to dry in open air - it should be placed in a beaker of acetone with expediency once removed from the resist-remover, and held by hand, using tongs to float the beaker in the sonicated environment for intervals of 5 seconds maximum. After each interval, imaging the diamond surface under microscope shows if sonication and liftoff have proven successful. It should be mentioned that the process of liftoff is immensely delicate and requires focus and finesse as it may compromise the the vdW device due to fluid agitation during liftoff.

3.5   Micro to Macroscopic Systems - Connection to an Atomically Thin Field Effect Transistor

3.5.1   Fabrication of a Diamond Anvil Circuit

Upon isolation of the electrodes the electrical connection may be routed to macroscopic system. The use of a circuit board is helpful as it provides an convenient base for soldering and routing conductive traces from the diamond to the outer electronics. Due to the metallic properties of the DAC, the contact area between the circuit board and the DAC should be made insulative to avoid the possibility of shorting any applied signal through the DAC. Figure 3.15 shows the top of a custom design printed circuit board (PCB) that allows for surface connection via conductive pads and features an insulative bottom for mounting to the interior of the DAC piston. The PCB routes the four leads to an area of the DAC where there is a structural vacancy in order to run wires out of the DAC and make connection to the bulk of the equipment.

To create electrical connection with the circuit board, traces may be cut from a roll of
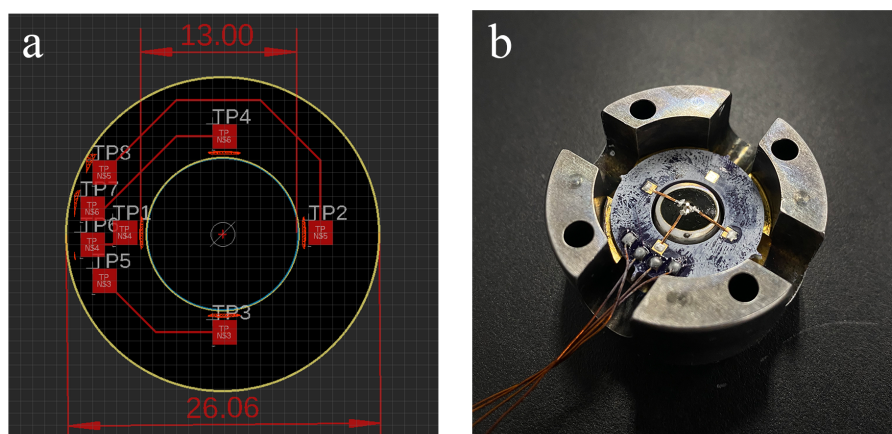
Figure 3.15: Surface pads on a custom designed insulative PCB. (a) Displays the schematic representation and geometry of a circuit board design that allows for intermediary connection to the sample. The PCB features 4 inner pads that are routed to the outer edge of the DAC piston chassis in order to make connection to wires that route signal into and/or out of the apparatus. (b) Shows a physical image of the PCB once it has been glued to the base of the DAC piston. The circuit is completed by running copper traces from the PCB pads up the backing plate base and painting silver epoxy up the facets to the EBD electrode pads. Copper wires connect to the outer PCB pads to route the signals to and/or from the measurement equipment. Dimensions of the design are listed in millimeters.

copper tape and epoxied along the interface of the PCB's electronic pads as they run up to the base of the diamond's pavilion. From that point, silver epoxy may be painted over the edge of the trace and make contact to the edge of the EBD electrode. The process is performed by hand under microscope with a medical-grade one-micron needle. Upon connection to each electrode, the DAC piston is baked in an oven for 1 hour to allow the silver epoxy to harden and cure. Meanwhile, down circuit, 28 AWG insulated copper wire may be sanded at the ends to expose the bare copper. One end may be soldered to the PCB as the other end is wire wrapped around a terminal pin.

Due to the potential to discharge accumulated static electricity, the DAC piston is held on a grounded bench top and should only be handled by a grounded individual. The DAC piston is, at this point, an electronic module capable of passing a current. The

applied signals are able to be applied through the sample once they are generated at the instrumentation. To maintain structural integrity of the connection to the circuit, an electronic base board was created to reduce tension on the wires as well as to create a modular base that could be retrofitted with a retainer that allows the DAC to be securely situated for axial optical measurements in different spatial orientations. The electronic base board contains female banana plug terminals for instrument connection as well as an earth ground tether for ensuring that the chassis of the DAC remains grounded during experimentation. Figure 3.16 displays the chassis of the electronic base board prior to being fit with terminals and cables.

3.5.2   Communicating with the Measurement Electronics

In order to apply a gate sweep to the atomically thin field effect transistor (ATFET), the tolerance of the device must be checked. Doing so provides the range in which an applied gate voltage will not contribute a significant leakage current through the dielectric layer of hBN to the drain of the device. In a three terminal system, commonly described by the gate, source, and drain of a field effect transistor, this may be completed by applying a forward bias through the gate to the drain and then through the gate to the source; and thereafter, performed with a reverse bias in the same configuration. It is a step-wise process begun by applying millivolts to the gate and going up to magnitudes of ± 5 V in steps of 100 mV. Observation of hundreds of picoamps indicates the voltages of reasonable limit as they may contribute fractions of nanoamps to the targeted measurements. Figure 3.17 indicates a strong linear dependence of gate voltage to drain current by perceiving the constant slope of the dielectric resistance. Both configurations during the gate-leakage checks measure a range of $50 - 55$ $G\Omega$ for the gate-to-source and gate-to-drain resistance, indicating the ability to perform the first experimental gate sweep for the vdW heterostructure.

Two power supplies are needed to apply signals, control, and measure a field effect
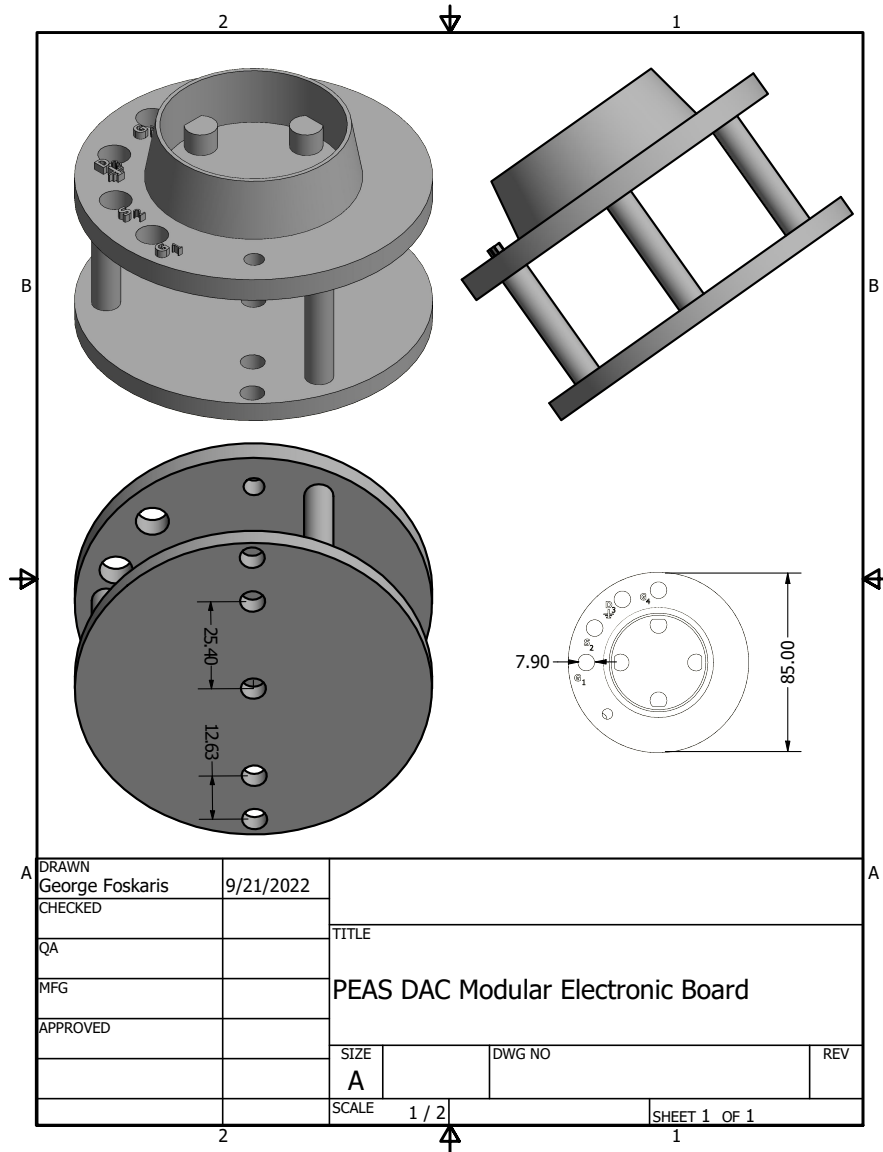
Figure 3.16: A modular base-board was created in order to orient the DAC on a stable, grounded bench top and minimize user contact with the electronics of the experimental apparatus. The base-board allows for controlled connection between the micro and macroscopic system which allow for transport measurements of van der Waals heterostructures in a DAC. The lower plate on the board features threaded holes for attachment to a grounded optical bench. The three columns create a chamber between the plates to maintain cables within the chassis. The top plate features female banana plug terminals and a grounding port that connects to the DAC. The beveled retainer, affixed to the top plate, features four inner plugs that lock the piston in place for microscope imaging. The beveled retainer may also be removed and replaced with a inverted triangular base-plate that may be used to orient the DAC horizontally (not pictured). The versatility of the modular board promotes the ability to obtain transport measurements alongside various in-situ optical measurements, if desired. Dimensions of the design are listed in millimeters.
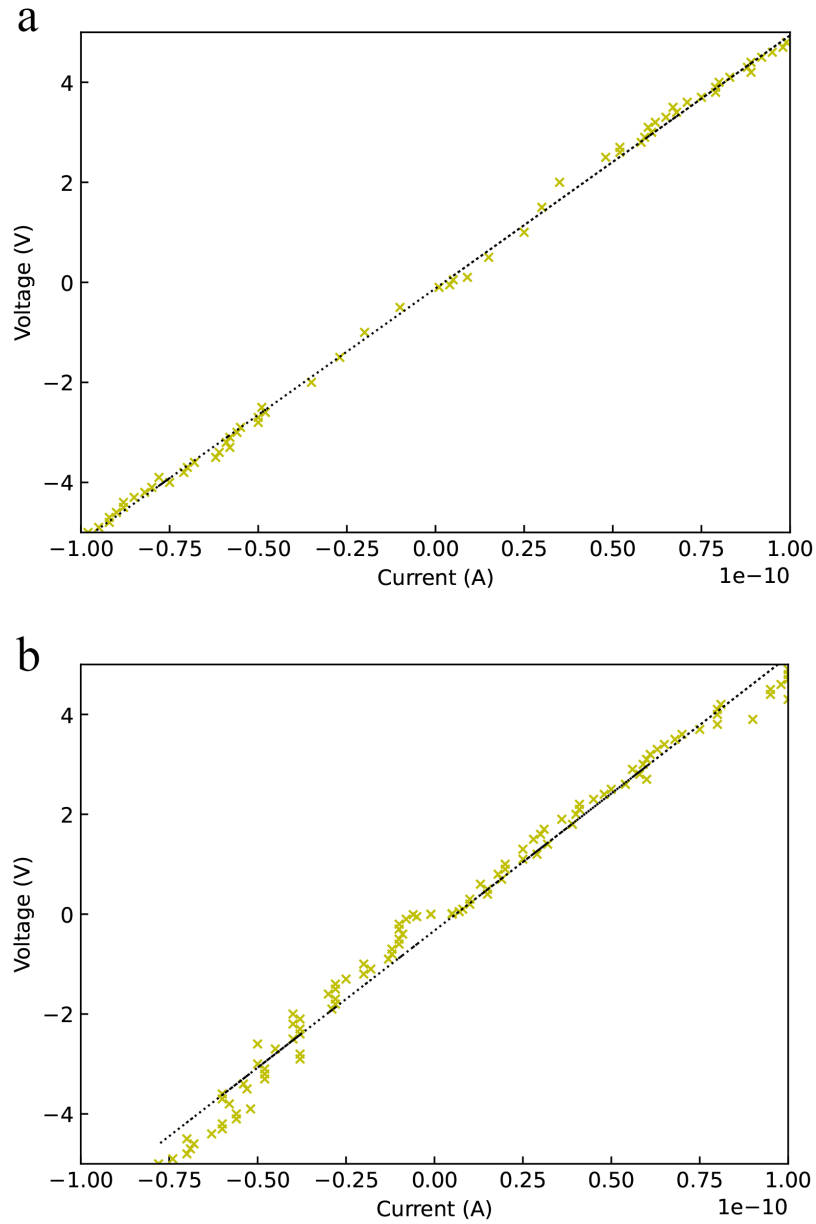
Figure 3.17: Gate voltage as a function of drain current. Ohmic behavior of the gate leakage current. The leakage check is performed by applying a forward bias from the gate terminal to the drain terminal in steps of ±100 mV up until the measured current regime is of hundreds of picoamps. The process is repeated with reverse polarity in the same way. (a) Displays the Ohmic behavior of the gate leakage current from the gate to the drain. The data has been fit with a linear regression and returns a resistance of nearly 55 GΩ between the graphite gate and the drain of the ATFET. (b) The data and applied fit from the graphite gate to the source of the ATFET. The graph indicates Ohmic behavior and provides a similar resistance of nearly 55 GΩ.

55

transistor. The schematic of the system used may be seen in Figure 3.18. One power supply controls the sweep voltage while the other is used to apply a constant voltage to the source and measure the drain current of the system. We use two Keithley 2400 series source-meters and control their outputs through a GPIB connection to the computer and a Python measurement protocol. The script is incredibly helpful as it navigates the measurement process to reduce the potential for user error. The exact script, seen in Appendix B, employs a 'for loop' to iteratively run the written code at specified intervals associated with the voltage-steps that compose the full gate sweep. Creating and applying the script to the instrument allows for hundreds of measured data points to be taken on the device in less than 90 seconds. This method offers a high throughput of data for analysis as well as improved consistency in the data collection. The initial sweep should be performed at ambient conditions to observe the electrical characteristics of the system in absence of applied mechanical pressure by which it measures a baseline standard for the electronic response of the vdW heterostructure via electric field effects. A photograph of the experiment in action may be viewed in Figure 3.19.

3.5.3   The Final System - Gas Loading a vdW Device in a DAC

Gas-loading of the system is performed by using a proprietary gearbox designed by Paul Ellison et al. [44]. It allows for the insertion of a nearly closed PEAS DAC into a cylindrical chamber constructed of steel with walls that are several centimeters thick [45]. As the DAC is suspended in the cylinder, different gases may be pumped into the chamber up to a pressure of 3 *kbar*. The initial pressurization of the chamber prior to closing the DAC offers the system an preliminary starting point in pressure and promotes the ability to reach the targeted pressure regimes. One of the primary benefits of a gas-loaded environment in a diamond anvil cell is that it may subject the system to a quasi-hydrostatic pressure environment. Depending on the gas employed as a PTM, deviations from hydrostaticity may vary up to tens of GPa; however, increasing the density
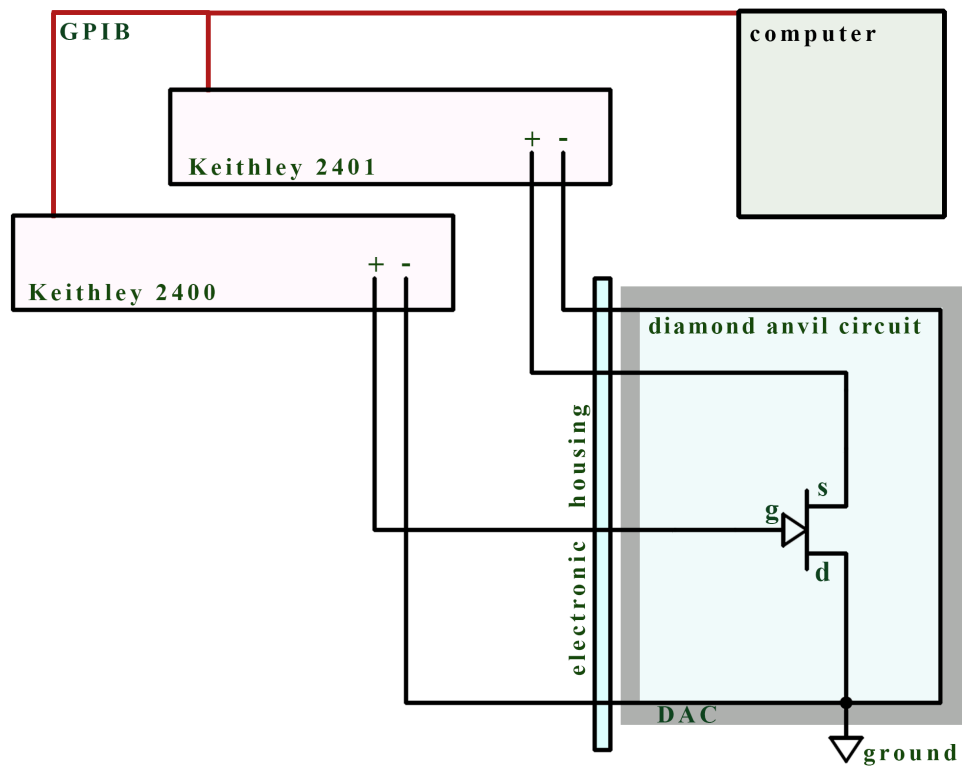
Figure 3.18: The functional schematic for the electronic measurements of van der Waals heterostructures in a diamond anvil cell. Using GPIB connections, a computer is able to control two Keithley 2400 source meters. Using a python script and configuration file, the applied voltage at the gate may be swept between the range of safe voltages found through the gate-leakage current tests. The connections are made from the instruments to electronic housing identified in baby blue. The connections that make their way to the sample from that interface are done so alongside a grounded DAC chassis, identified in grey. The voltage bias applied at the source is held constant during an iteration of the gate sweep and may be modulated thereafter to obtain other drain current data sets for the ATFET. Once the device has been characterized at a given pressure, the DAC may be compressed to obtain a new data set on the electronic response of the system at new pressures.

of fluid media in the sample chamber is of primary interest. Indeed, gas-loading may offer other useful advantages such as providing a desired reactive environment in the sample chamber of a DAC. For example, when employing molecular H_2 gas, as seen with pressure experiments on hydrides in a DAC, the hydrogen PTM may offer the system a chemical pressure that may synthesize new materials when utilized alongside mechanical [46].

Depending on the systems in question, it could be useful to employ certain gases that yield inert reaction environments as well as uniform hydrostaticity upon compression. Understanding how evenly the pressure environment is distributed in the sample chamber would be important in studies pertaining to deviatoric stress. In comparison, a chamber loaded solely with a dielectric, like alumina, does not offer a pure hydrostatic pressure environment; however, it offers the use of an insulating PTM that is equipped to minimize the gasket's tendency to flow inward/into the sample chamber, which is a common occurrence as the DAC engages in uni-axial compression. We seek to employ Argon gas, as it is inert/nonreactive as well as compressible such that it creates a quasi-hydrostatic, environment up to tens of GPa; therefore it is a useful initial fluid medium to study our vdW devices under pressure for the first time. Whatever choice is made for the functional PTM, it should cater to the experimental questions being asked and offer the least amount of uncertainty.
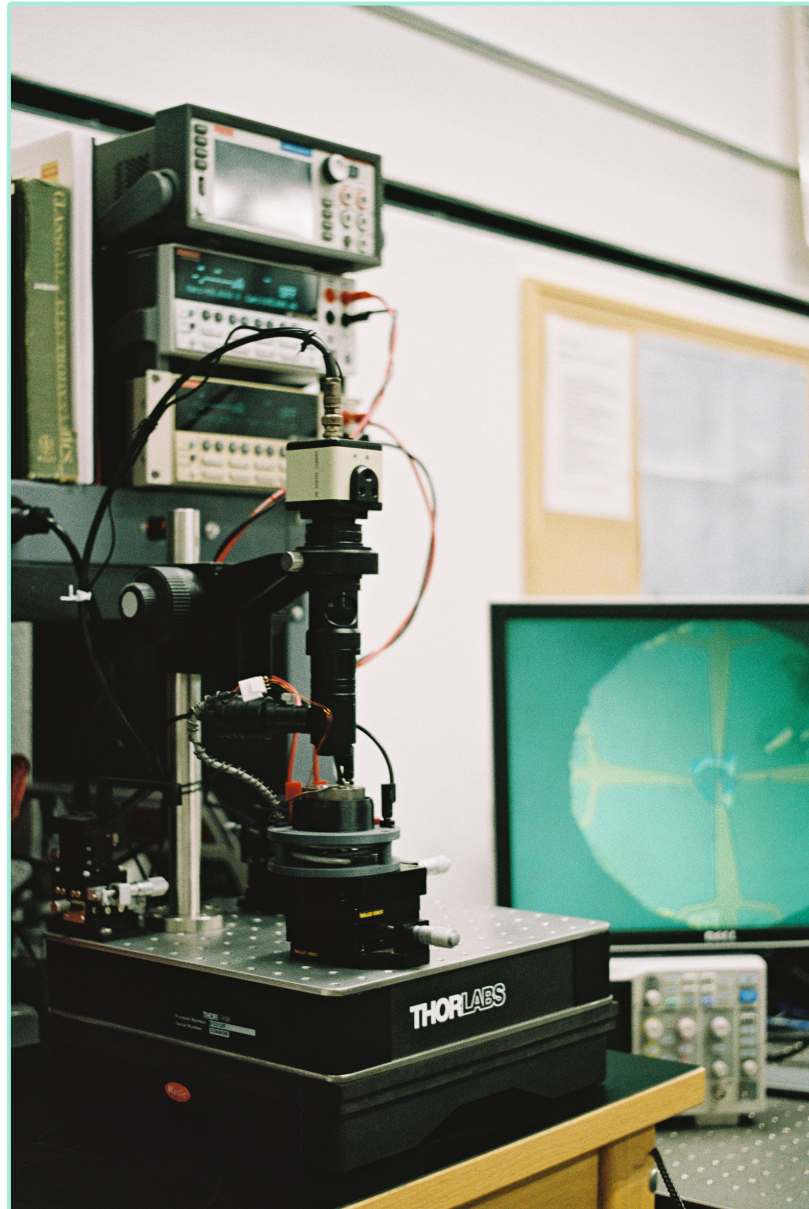
Figure 3.19: A photograph of the measurement bench. The foreground features the grounded bench top, translation stage, electronic baseboard and DAC assembly, which is in connection to the two Keithley 2400 Source Meters in the upper background. The screen is used for in situ monitoring of the ATFET during transport measurements and displays a digital image of the vdW heterostructure on the monitor.

Chapter 4

Results

The methodologies described in Chapter 3 may be applied to deposit electrodes directly on a diamond anvil substrate with or without a vdW heterostructure. The trials and errors of the methodological developments therein led to some empirical results, which were previously discussed. In total, the multiple iterations of instrument itself produced a few measurements on different systems pertaining to bulk polycrystallines and 2D materials. This chapter will present and discuss those signals from the basis of the materials in study. As the first successful milestone of depositing pre-patterned electrodes to a diamond surface had been achieved, and the course to study a vdW heterostructure sample in a gas-loaded PTM had not yet been realized, the project was in need of a benchmark test. To investigate the electrical integrity of the 100 nm electrodes deposited to the surface of a diamond anvil, the research began by verifying the electronic response of polycrystalline MnS_2 loaded in the cell and transport measurements were studied under pressure.

4.1 The Resistance of Polycrystalline MnS$_2$ - Electrodes at Pressure

The choice to study MnS$_2$ was made for a few reasons. The most apparent came from a recent study by Durkee, et al. [7]. The study employed transport measurements to show that the electronic response of polycrystalline MnS$_2$ exhibited an large, apparent drop in resistance over a modest 12 GPa pressure regime in a DAC. The apparent drop in the resistance made it an excellent candidate for the benchmark test on the electrodes as the previous study was also performed on site, and was well understood. Thusly, a sample of MnS$_2$ was powdered via pestle and mortar and the studied by utilizing a pressure transmitting medium of Al$_2$O$_3$ (alumina) that was packed entirely into the hollowed gasket and seated to the cylinder diamond. A small cavity was then bore into the alumina. The polycrystalline MnS$_2$ was packed into that cavity and the chamber was subjected to pre-compressions in order to homogenize the sample thickness at the culet faces.

Lithography, EBD, and electrode liftoff were successful and produced an eight probe pattern that extended across the culet and down the pavilion of the diamond. The culet of which may be seen in Figure 4.1. Four electrical connections were crafted to the four of the eight electrodes using silver epoxy, traces of copper tape, protoboard, and solder. A ruby was placed on the culet face and the DAC was closed. An initial measurement using ruby florescence indicated the nearby chamber was at a pressure near 0.84 GPa [47].

A four probe electrical measurement at 0.84 GPa verified the linearity of ohmic behavior of the sample and yielded a resistance of approximately 150 $k\Omega$ when biased in a range between ± 10 V, seen in Figure 4.2 (b). Ruby florescence measurements yielded an increase in pressure at every iteration of DAC compression. Figure 4.2 (a) displays the corresponding transport data as a function of pressure from this study and compares it to recreated data from the Durkee study (data presented with authors' permission). The trend between both studies is similar and approximately displays a four order drop in resistance
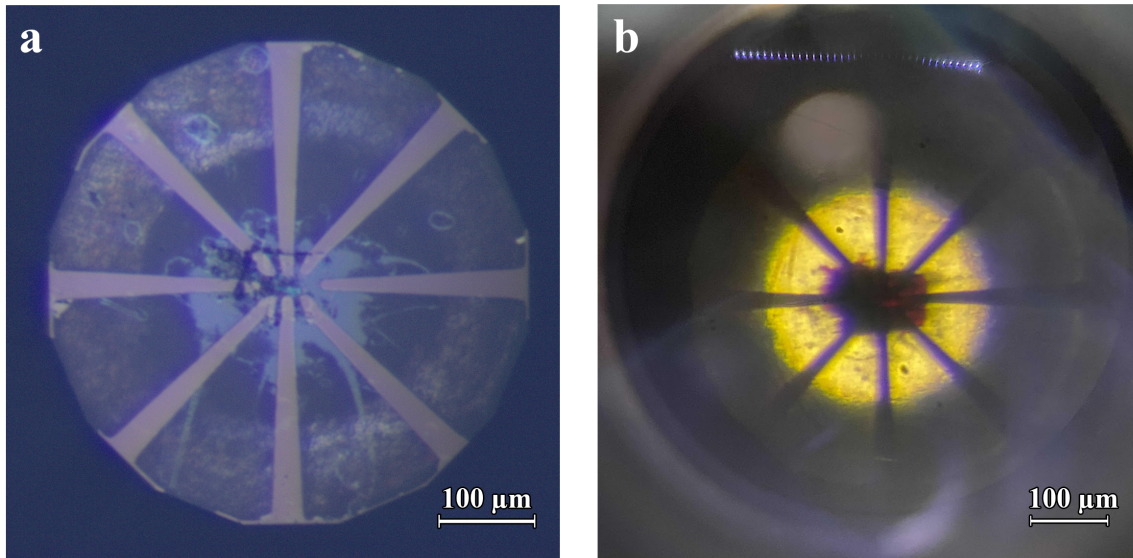
Figure 4.1: Images of a diamond anvil cell loading of MnS_2 and eight electrodes. (a) A 500 μm culet at the piston is imaged through the table of the diamond. The surface of the culet is visualised with the insulating gasket near the outer perimeter of the diamond. The dark, central location identifies the powdered alumina in the chamber. The light grey material at the center identifies the polycrystalline MnS_2. The sample chamber near 15 GPa. (b) A transmission image of the same loading from the same perspective, highlighting the reddish hue of the MnS_2.
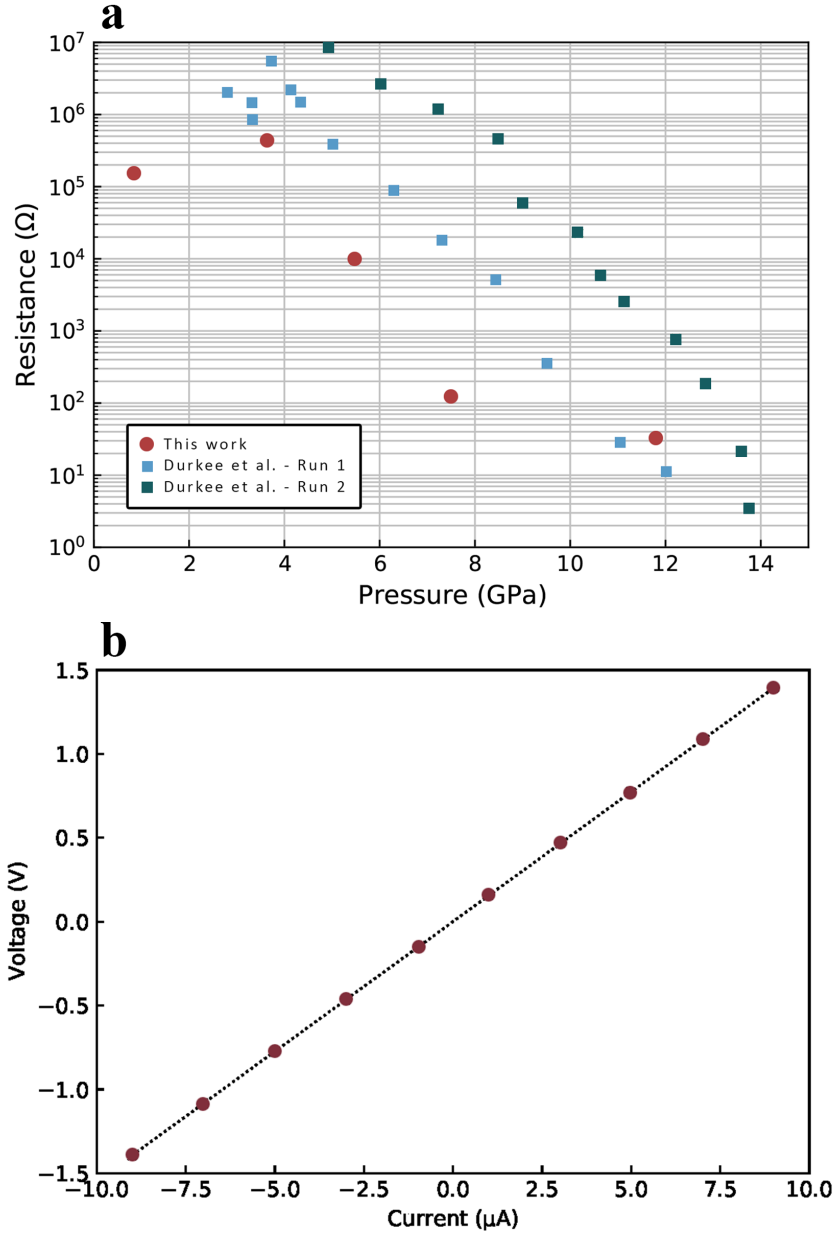
Figure 4.2: Resistance graphs of polycrystalline MnS_2 in a DAC. (a) Applied pressure induces a drop in resistance of MnS_2 due to the properties of a negative charge transfer insulator; upon the volume collapse, an electron is donated from the valence band to the σ^* conduction band. The sample is in mixed phase throughout the pressure regime up to 12 GPa. Our study observes a four order drop in resistance and is shown alongside data from the Durkee et al. study [7], which has been recreated and displayed with authors' permission. (b) Near 0.84 GPa, Ohmic behavior is seen from the linear dependence of measured voltage to applied current when a four-terminal transport measurement is configured to the sample.

when subjected to compression up to nearly 12 GPa. Recalling, the resistance of a material is dependent on the spatial dimensionality of the sample; therefore, the difference in the data spread between the two studies may be attributed to the form in which the data is graphed. Furthermore, the maximum drop seen in the Durkee study is nearly eight orders of magnitude around 12 GPa; however, the minimum drop in resistance along the same pressure regime is close to five orders of magnitude. Overall, the acquired signals from the sample trend with the literature where the four order drop in resistance in our study may also be attributed to the behavior of a negative charge transfer insulator, whereby the induced pressure on the sample creates a density-driven volume collapse such that an electron is transfered from the valence band to a σ^* conduction band. The collapse therein yields mixed phasing and partial metallization of MnS_2 up to pressure regimes greater than 30 GPa. At ambient pressure, p-MnS_2 is considered to be an insulator of pyrite phase ($Pa\bar{3}$) and upon compression, it begins to shift into a metallic, arsenopyrite, ground state phase α-MnS_2 ($P2_1/c$). The electronic density of states in the conduction band raises as the Fermi energy increases and breaches into the conduction band, tightening the electronic band structure. It is reported that a full metallization of α-MnS_2 is approximated to be near 50 GPa, whereby the system is fully collapsed in arsenopyrite phase.

The study subjected MnS_2 to a final pressure near 15 GPa as measured through ruby florescence; however, the transport signal was lost to sample above 12 GPa indicating a compromised circuit. It was assumed that the electrodes were severed upon compression; however, the location of the failure is unknown as the leads are not recoverable upon opening the DAC. The electrical connection to the sample was completely compromised and the 100 nm electrodes patterned to the diamond anvil are left as scraps of conductive media. Overall, the results from the MnS_2 test indicated that the 100 nm thick electrodes were capable of bridging an electrical connection through the culet-pavilion interface as verified from the MnS_2 transport signals, and the integrity of the leads proved useful up into pressure regimes near and above 10 GPa, which was of interest for future experiments.

4.2 Fragility and Control of a van der Waals Device on a Diamond

The methodologies described in Chapter 3 and Figure 3.5 of exfoliation and stacking the flakes to create vdW device allowed for transfer of an ATFET to the culet of a diamond anvil. Upon transfer, the hBN appeared to cleave. Although, the cracks were present on the hBN substrate, nearly all the bilayer graphene was situated on a homogeneous piece of the hBN; therefore, it was projected to have little external effect when gating the device. The device featured bilayer graphene at its surface, an hBN dielectric, and a graphite gate.

The resistance of the bilayer flake in the vdW heterostructure was measured using a two terminal method. Applying 10 mV to the source and measuring a signal near 1.15 μA of current through the bilayer graphene drain yielded a reasonable resistance of 8.73 $k\Omega$ for the sample. During the gate leakage tests, the applied voltage to other terminals of the ATFET yielded measured current signals that became increasingly weak. Upon visual verification, it was easily determined that the sample itself had been compromised. In Figure 4.3, (a) and (b) show the quality of the heterostructure before and after failure, respectively.

The sample was believed to have been subjected to some form of electrostatic discharge. The basis on which the assumption was adopted are due to the functional qualities of the instrument at this point in the research. The applications of grounding the DAC, bench-top, user, and any components in contact with the insulated wires, or DAC chassis itself had not yet been implemented. Furthermore, protoboard was used as the base for the circuitry; therefore, there is also a possibility that a pathway of conduction had formed from the DAC chassis to any of the four possible contact points and/or traces that were soldered to the circuit. The base of the protoboard had been fully covered in insulative epoxy by hand, therefore, it may be possible that an electrical pathway was formed through fabrication error.
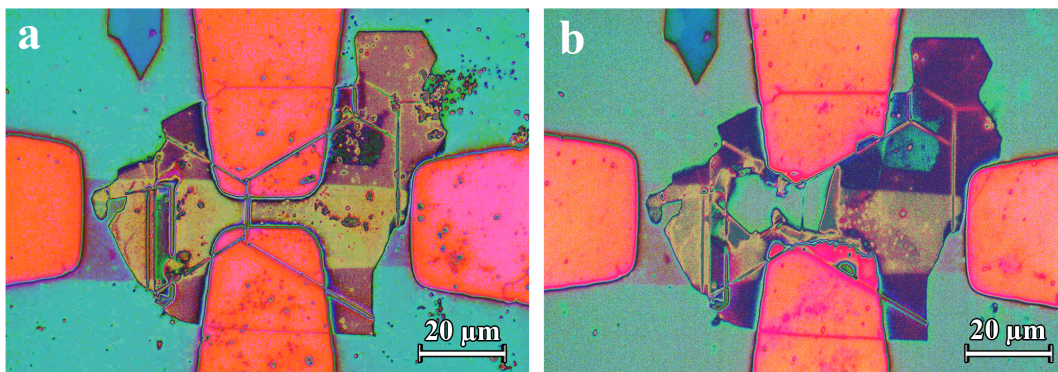
Figure 4.3: Enhanced images of four electrodes made in connection to a vdW heterostructure on a diamond anvil before and after destruction. The conductive electrodes are visualized in orange-pink. (a) The device features bilayer graphene at its surface (shadowed in the center), hBN as a dielectric (larger polygonal shape, cracked), and a graphite gate (horizontally oriented, light-purple hue at edges and yellowish hue under the hBN flake). (b) The compromised device shows destroyed electrode tips disconnected from the sample. It is evident that the diamond culet (aqua-blue) is revealed in the center of the device. Discharge may have occurred through the cracks in the hBN.

Due to the failure of the device, the research was set to modify the approach in order to promote and retain sample integrity, and reduce the potential for electrostatic discharge to make its way through the heterostructure of the system. It was at this stage that the custom designed PCB was created to feature surface pads and a purely insulative bottom, as seen in Figure 3.15. In addition, it was realized that a electronic base board would serve useful in order to minimize user error and improve the ergonomics and control of applying signals to the device.

4.3 Graphite-Gated Conductance of Bilayer Graphene in a Diamond Anvil Cell

The last of the vdW heterostructures assembled that was successfully transferred featured a flake of bilayer graphene at its surface, an hBN dielectric, and a graphite gate. Enhanced microscope images displaying the product of the full fabrication process is shown in Figure 4.4 (a) - (d) before compression in the diamond anvil cell. The task of creating electrical connection to the device was successful using the electrode design seen in 3.9 (c). The post-lithography processes allowed for a 3 terminal connection to the ATFET. The drain and source electrodes, as referenced to the circuit diagram seen Figure 3.18, was made in contact over the bilayer flake. The python script set to control the sweep iterations was calibrated and tested on a MOSFET 620 integrated circuit before connection was made to the device and studied; it may be seen in Appendix B.

The bilayer graphene flake displayed ohmic behavior when tested through a 2 terminal measurement in the applied potential range of $\pm 5\ mV$, seen in Figure 4.5 (b). The measurement was made in the absence of a perpendicular electric field set by the gate, and is indicated by the finite conduction presented at the null gate voltage as seen in Figure 4.5 (a). The measured resistance of the bilayer graphene sample was reasonable, near $16.7\ k\Omega$. The gate leakage tests, as performed in 3.17, allowed for a confident sweep of $\pm 5\ V$
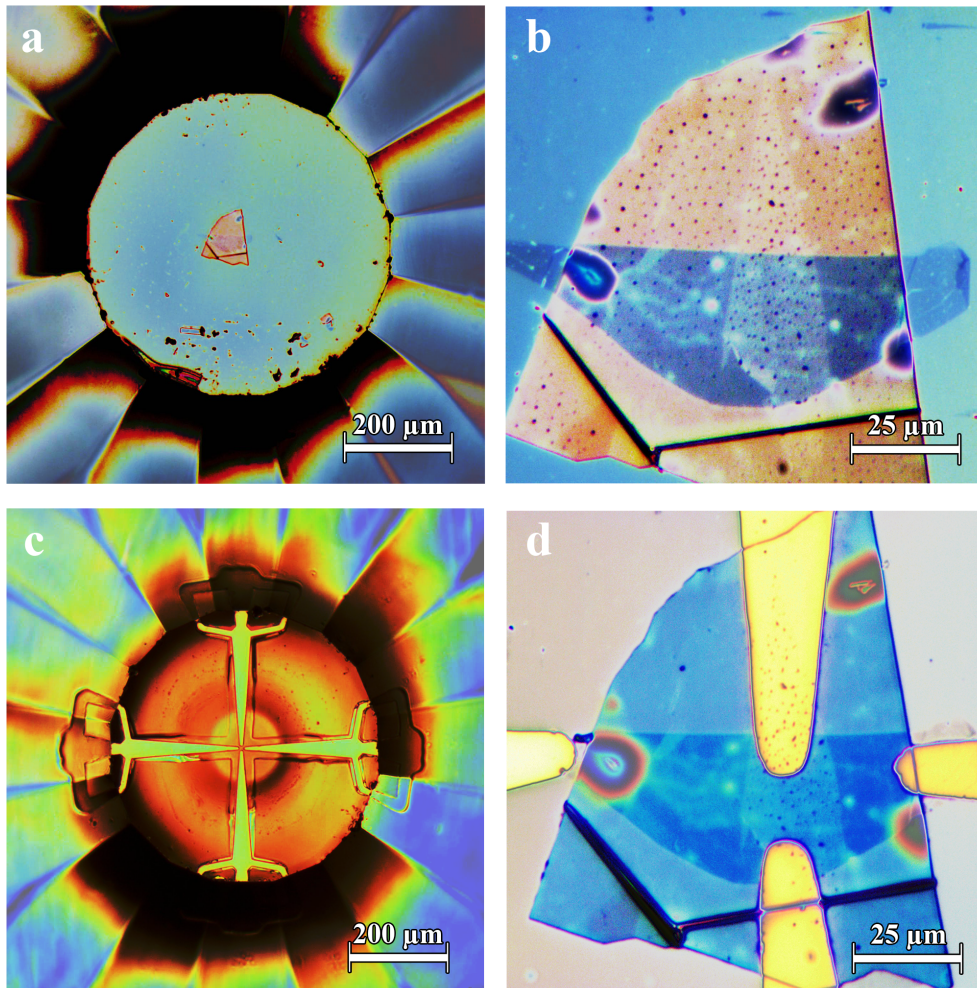
Figure 4.4: Enhanced microscope images a transferred ATFET and the fabrication of electrodes on a diamond anvil substrate.(a) Displays a vdW heterostructure transferred directly to to a 550 μm culet at 5x magnification. (b) The three layer ATFET at 50x magnification. The horizontal flake is the graphite gate (blue), the larger flake is the hBN (beige), and the vertical flake in the center is BLG (off-white). (c) Electrode pattern on the diamond anvil at 5x magnification. (d) Post-fabrication of the electrodes to the ATFET at 50x magnification. Notice the electrodes in connection to the bilayer graphene perpendicularly overlap with the graphite gate. Both electrodes to the left and the right of the image are in connection to the gate - one of them is redundant and used a back-up.

68

through the graphite gate to the device considering the contribution of the gate potential only increased the drain current by hundreds of picoamps. The source voltage was held constant at 5 mV without damaging the device during the gate sweep. The conductance curve of the device at ambient pressure may be seen in Figure 4.5 (a) and features an averaging of 200 data points over three identical sweeps of the gate voltage. The parabolic fit may be used to describe the conductance of bilayer graphene near the charge neutrality point when interpreted through the Boltzmann model in the Born approximation.

The approximation indicates that the driving field is the mechanism that is responsible for scattering. This may be attributed to the incident electric field on the sample. The approximation is also considered most valid for long range disorder in the bilayer flake where the scattering due impurities in the lattice are less abundant. Furthermore, the most realistic representation of the conductivity of the system should take into account the effects of Coulombic screening, or Coulombic repulsion between the electrons themselves. It has been shown theoretically that the conductivity of single layer graphene and bilayer graphene is dependent on the density of charge carriers [48] such that through the Boltzmann transport model, there is a finite charge density that describes when the conductivity is best approximated to be linear, or best described as parabolic. Typically, the conductivity of single and bilayer graphene systems is directly proportional to the number of charge carriers, $\propto n$, i.e. linear as it trends away from the charge neutrality point (CNP); however, near the CNP, the conductivity of BLG due to screened Coulombic disorder should display proportionality more like $\sigma \propto n^{\alpha}$, where $1 \leq \alpha \leq 2$ [49]. Xu et al., obtain an analytical expression for a limiting charge carrier density, n_o, and define it as $n_o = \frac{1}{3\pi a} \left(\frac{\gamma_1}{\gamma_o} \right)^2$. Here, the gamma parameters are the same that were previously presented and described in Chapter 2 and maintain constant values such that $\gamma_o = 2.8 \ eV$ and $\gamma_1 = 0.4 \ eV$. Above the limiting charge carrier density, $n > n_o$, the conductivity of BLG is approximated to be linear such that $\alpha \to 1$, but below this limit, $n < n_o$, the conductivity is approximated to be parabolic such that $\alpha \to 2$ [48]. It must be recognized
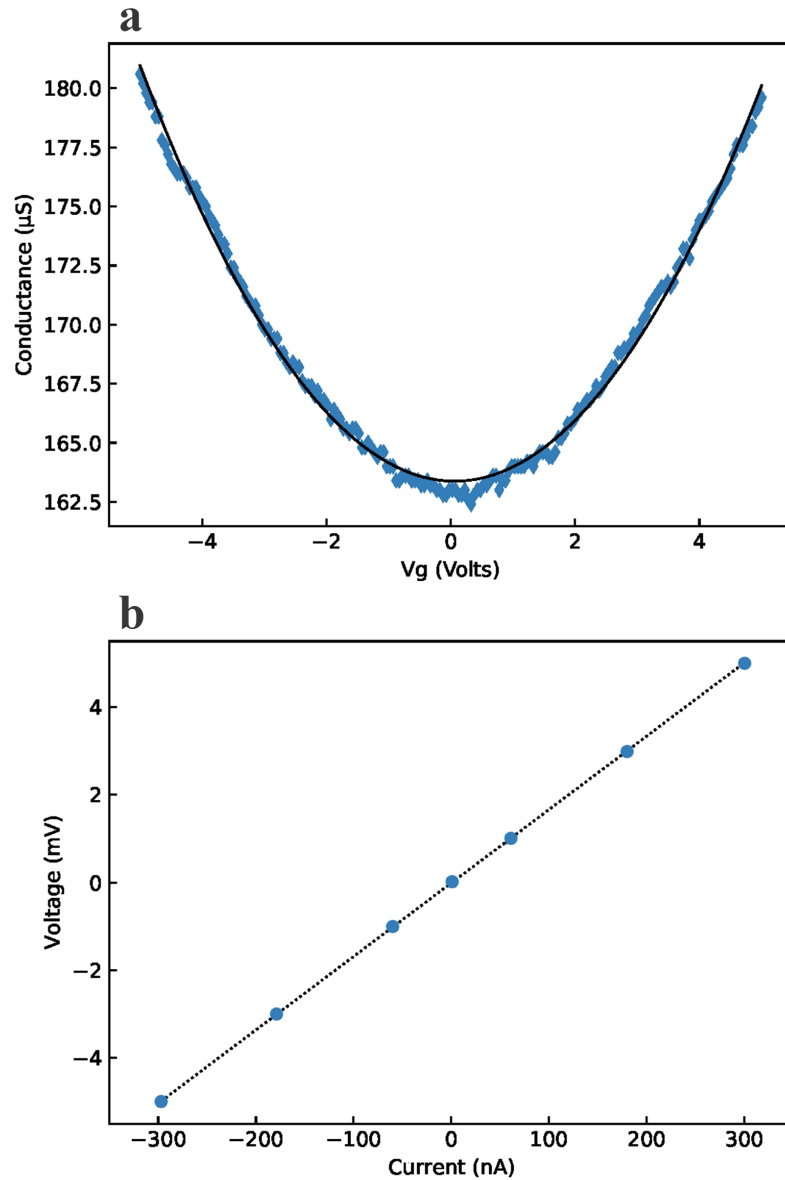
Figure 4.5: Electrical response of bilayer graphene vdW heterostructure with and without a gate at ambient pressure. (a) The data displays 200 data points averaged over three accumulations of the $\pm 5\,V$ gate sweep on the ATFET. The parabolic fit to the data indicates a course approximation of the conductance of the system near the charge neutrality point. (b) The ohmic behavior of the bilayer graphene in absence of a perpendicular electric field. The linear dependence on the measured voltage when applying a current bias in a two terminal measurement is evident. The slope yields nearly $16.7\,k\Omega$ of resistance in the bilayer graphene flake between the source and drain electrodes in ambient conditions.

that the number of charge carriers is capable of being tuned and that they may be abundantly available to the BLG sample in the vdW device under certain conditions. Recall that if a positive bias is applied to the gate, it produces an electric field that orients perpendicularly through the vdW device; the product of which allows the ATFET to open the negative channel between the source and drain of the BLG, thereby increasing the magnitude of negative dopants directly, which increases the conductivity and may be measured directly in a variety of electrode configurations.

Once the electrical response of the vdW heterostructure was measured in the three terminal arrangement, the DAC was loaded with a ruby and the initial signal from its fluorescence was obtained for ambient conditions. The DAC was nearly sealed and loaded into the on-site gas-loading chamber. Argon gas was set to fill the environment at 3 *kbar* and the on-site loading mechanism used to close the DAC was employed. Under supervision, visualisation of the chamber indicated that the alumina PTM began to compress and run towards the center of the culet. At 3 *kbar*, the argon gas-loading was not sufficient enough to hold the gasket back from creeping in toward the sample at the culet center. Further compression needed to close the DAC in the pressurized chamber was stopped under the impression that the DAC may have been closed and/or isolated from the outside environment. The visual aid of an interference pattern between the outer culet and stainless steel gasket was identified, but was difficult to discern due to the limited the field of view of the supervision camera. Upon removal of the DAC from the gas-loading chamber, a ruby florescence measurement in the sample chamber verified that the signal had not shifted up in energy, which was to be expected if the chamber had been sealed at 3 *kbar*. The gas-loading was unsuccessful and upon visual verification, the electrodes leading to the vdW device appeared sheared and broken. Connecting the device to electronic baseboard and applying the Python script to sweep the gate to acquire signals from the system's drain verified the absence of electrical connection to the device as the readings displayed background noise.
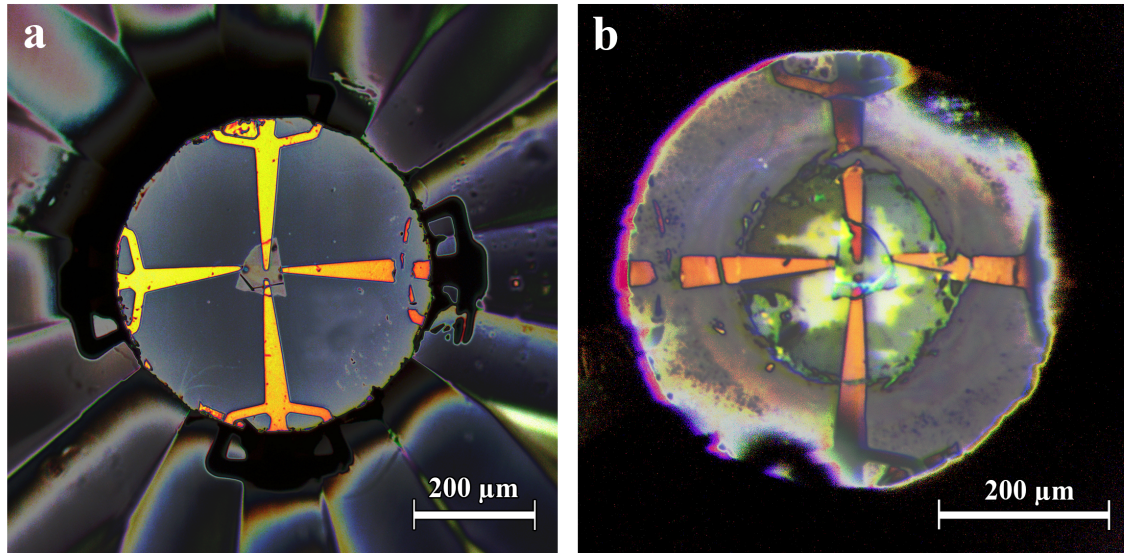
Figure 4.6: Enhanced images of four electrodes made in connection to a bilayer graphene vdW heterostructure. (a) Displays a microscope image of the transferred device before gas-loading. The device was was measured on the piston in ambient conditions without full assembly with the cylinder. The image displays a three terminal electrode pattern. The four electrode, seen on the right was sheared during fabrication, luckily, the connection it would have made to the gate of the device was redundant. (b) Displays the quality of the ATFET and sample chamber after compression and gas-loading. The outer perimeter of the gasket and alumina are differentiated by a subtle hue of grey. The area in which the alumina dielectric crept to may be identified by the irregular material encompassing the area near the inner device. It is easily seen that many of the leads have been broken near the edge of the precompressed alumina and along the region that it ran upon compression in the gas-loader.

Chapter 5

Conclusion and Future Work

5.1 Overview

In general, we have shown it is possible for techniques of photolithography and electron beam deposition to be employed to superficially deposit electrodes on a diamond anvil surface whereby the electrical measurements on atomically thin van der Waals heterostructures may be studied in response to external electric field and, eventually, applied pressure. The transformation of a DAC into the instrument capable of these measurements is dependant on the fragility and integrity of the electronic pathways therein; which is forefront and apparent as the dielectric materials used to insulate the gasket have presented complications during compression. The resulting functional instruments produced may be recreated through the empirical metrics tabulated in Appendix A, Tables 1 - 2. We have presented a theoretical foundation affiliated with monolayer and bilayer graphene structures in the tight-binding approximation in order to create a framework for which the material response may be understood from the basis of its pristine ground state. Scaling the system up, we have also shown that the charge carrier density and conductivity of bilayer graphene may be better understood in the Born approximation when the transport mechanisms are analyzed through the Boltzmann

transport model, such that in the presence of electric field effects, BLG is subject to a carrier density limit that provides the bounds to approximate the characteristics of the band structure near the high symmetry K and K' points of the Brillouin zone.

Experimentally, the initial benchmark test on a bulk MnS_2 proved that techniques employed to deposit the electrodes on the surface of diamond were functional up to a pressure near 12 GPa in a DAC by verifying the distinct characteristics of the sample upon compression. The quality of the experimental apparatus at that time was subject to the the poly-crystalline PTM of alumina and epoxy, which ultimately aided to reduce PTM flow under compression in a non-hydrostatic environment. In contrast, when the same technique was applied in efforts to study a bilayer graphene vdW heterostructure, a similar method of creating a dielectric gasket was the source of the electrode failure due to the sample chamber being partially packed with the insulative dielectric and the fragility of the electrodes themselves. Further efforts to create a functional dielectric gasket in a DAC could be explored in conjunction with prepatterned electrodes. The task at hand requires that the dielectric gasket dually seals the chamber of the pressure cell without offering excessive flow into the sample chamber upon compression as to not shear the prepatterned electrodes, and it must remaining insulative to keep the superficial leads from short circuiting to any metallic media. An empirical solution to create a useful dielectric gasket that offers the ability to achieve pressure dependent transport measurements on vdW heterostructures is still to be determined, but is seemingly close should more time be spent on the matter.

These results have offered pathways and insight into the procedural tasks that will allow for electrical transport studies on van der Waals heterostructures in a diamond anvil cell. The exploration of these materials at extreme pressures could lead to new discoveries, and is of relevant interest in other recent studies. Should the research continue in this capacity, it could be useful to apply techniques seen in other research on 2D materials in a DAC. Studies by Ke, and Chen, et al. [23, 50], successfully employ a polycrystalline

powder of cubic boron nitride as the insulative gasket dielectric in a DAC; however, they improve the structural integrity of the leads through the placement of platinum foil, of 2 μm thickness, at the edge of the culet-pavilion interface in order create a shoulder for the electrodes at the compression edge of the gasket. This technique was also recently employed by Dasenbrock-Gammon on single layer graphene in a DAC [36], whose study explored the resulting resistance of graphene as a function of pressure through transport, concluding that the resistance of single layer graphene is marginally effected by uniaxial strain offered by the DAC due to c-plane stiffness of the hexagonal structure.

In general, material research on 2D materials in pressure environments is currently of high-interest and there does not exist an abundance of literature on the various effects associated with pressure applications. The complexity of the experiments themselves also vary greatly as nearly every group offers a novel methodology to transfer, or grow, the 2D materials to a diamond anvil surface, or other type of pressure cell. Furthermore, most studies offer different methods for making electrical contact to the samples, if at all. The commonality between this research, and the experiments that exist on its periphery, is the exploration to find new science on 2D materials at pressure, as up to now, the science of 2D materials has offered new pathways to potentially create smaller, faster, and more efficient electronics through the understanding of applied quantum electro-dynamics. Experiments on 2D materials may change the way we utilize electronics in the world. It is possible that in time, this study could lead others to new breakthroughs for applications of vdW devices in society. Surely, the avenues to any potential discoveries are going to be clouded, not only by the limitations of the physical apparati, but through approximation, uncertainty and the ever present conception that there will always be more at play than may be accounted for, but there is hope still that despite these restraints there will be a path for which humankind may explore and find answers to questions that we have yet to ask. That with enough time, the precision of our knowledge will increase. In the end, you may dive deeper every day, never to find a bottom.

Appendix

A Cleanroom Metrics for Diamond Substrate Processing

Table 1: Photosensitive Polymer Metrics

Type	Spin (RPM $\times$ s)	Thickness (µm)	Cure (°C $\times$ s)
LOR	1000×20	1	150×9000
AZ4110	2000×20	2	95×6000

Table 2: Photolithography on Diamond Metrics

Recipe	10x Exposure (s)	2.5x Exposure (s)	Development (s)	DI Rinse (s)
Single	0.8	3.0	60	30
Bilayer	1.7	5.5	60	30

Table 3: Electron Beam Deposition Metrics

Metal	Pressure (torr)	Applied Current (mA)	Target Deposition (Å/s)	Thickness (nm)
Cr	6×10^{-6}	$30 \leq I \leq 40$	0.5	10
Au	6×10^{-6}	$50 \leq I \leq 80$	1.0	90

B Python Scripts to Connect and Operate Two Keithley 2400 Series Sourcemeters from a Terminal

Part I: Connection

```
from qcodes.instrument_drivers.tektronix.Keithley_2400 import Keithley_2400
sm01 = Keithley_2400('sm01', 'GPIB0::24::INSTR')
sm00 = Keithley_2400('sm00', 'GPIB0::23::INSTR')
```

Part II: Configuration

```
# Config file for Gate Sweeps at Varying Source Bias Voltages
# Keithley: sm01 controls the Gate, sm00 controls the Source
# George Foskaris & Justin Alvarez 08/03/22
file:
    exp_name: 'DAC_vdWHeterostructure_Gate_Sweep'
    sample_name: 'DeviceName_SweepNumber_Date'
#Gate Range and Steps for the Keithley 2401 aka sm01 in Volts
gate1_rng:
  - -5
  - 5
gate1_steps: 200
#Bias Range and Steps for the Keithley 2400 aka sm00 in Volts
bias_rng:
  - 0.005
  - 0.005
bias_steps: 1
#Delay between steps of the fast axis
delay: 0.1
```

Part III: Operation of Gate Sweep, Live Plot, and Save

```
import qcodes as qc
from qcodes import initialise_database, load_or_create_experiment, Measurement
from qcodes.data.location import FormatLocation
from qcodes.data.io import DiskIO
```

```python
from qcodes.plots.pyqtgraph import QtPlot
import yaml
import numpy as np
import time
import os, sys, inspect


currentdir = os.path.dirname(os.path.abspath(inspect.\\ getfile(inspect.currentframe())))
parentdir = os.path.dirname(currentdir)
sys.path.insert(0, parentdir)
delay = 0.2


gate_read = sm01.volt.get
source_read = sm00.volt.get
current_read = sm00.curr.get


# Ramp the Gate Voltages from Current Magnitude to voltage_sweep_range[0]
(sm00 and sm01)
def protective_ramp_sm00(tempvi, tempvf):
    if tempvi == tempvf:
        return
    step = 21
    v_steps = np.linspace(tempvi, tempvf, step)
    #delay = 1
    for jj in range(step):
        Vs = v_steps[jj]
        sm00.volt.set(Vs)
        time.sleep(delay)
    time.sleep(0.2)
    return


def protective_ramp_sm01(tempvi, tempvf):
    if tempvi == tempvf:
        return
```

```python
        step = 21
        v_steps = np.linspace(tempvi, tempvf, step)
        #delay = 1
        for jj in range(step):
            Vg = v_steps[jj]
            sm01.volt.set(Vg)
            time.sleep(delay)
        time.sleep(0.2)
    return


def main():
    # Open the config file
    with open("Z:\\George\\Location_of\\gate_sweep_config.yml", 'r') as ymlfile:
        cfg = yaml.safe_load(ymlfile,)

    # Load the Variables from Config file
    e_name = cfg['file']['exp_name']
    s_name = cfg['file']['sample_name']
    gate1_vsteps = cfg['gate1_steps']
    gate1_rng = cfg['gate1_rng']
    bias_vsteps = cfg['bias_steps']
    bias_rng = cfg['bias_rng']
    tot_steps = gate1_vsteps*bias_vsteps
    delay_meas = cfg['delay']

    #Define the Range for the Gate and Bias sweep
    gate1_steps = np.linspace(gate1_rng[0], gate1_rng[1], gate1_vsteps)
    bias_steps = np.linspace(bias_rng[0], bias_rng[1], bias_vsteps)

    #Name the Experiment and Sample
    exp_name = e_name
    sample_name = s_name
```

```python
#Create the database
folder = "Z:\\George\\Python_Scripts"
qc.config["core"]["db_location"] = folder + '\\experiments.db'
initialise_database()
exp = load_or_create_experiment(e_name,s_name)
folder_loc = folder + '\\data\\{date}'
loc_fmt = folder + '\\data\\{date}\\#{counter}_{name}_{sample}'
rcd = {'name':e_name, 'sample': s_name}
loc_provider = FormatLocation(fmt=loc_fmt)
loc = loc_provider(DiskIO(folder), record = rcd)
filepath = loc
if not os.path.exists(filepath):
    os.makedirs(filepath)


#Check if Outputs are on: If so, Ramp to Turn off the Keithleys:
if sm00.output():
    temp_v3 = sm00.volt.get()
    protective_ramp_sm00(temp_v3, 0)
    sm00.output(0)


if sm01.output():
    temp_v4 = sm01.volt.get()
    protective_ramp_sm01(temp_v4, 0)
    sm01.output(0)


#Physically Observe the Compliance Shift, you have 5 seconds:
time.sleep(5)


#Set the Compliance at Each Iteration
sm01.compliancei(105e-6)
sm00.compliancei(105e-6)
```

```python
#Physically Observe the Compliance Shift again, you have 5 seconds:
time.sleep(5)


#Turn the Keithley inputs on:
sm01.output(1)
time.sleep(delay)
time.sleep(0.2)
sm00.output(1)


#start the Time
t0 = time.time()


print('Ramping_to_start_voltages,_please_wait')
tempv = source_read()
protective_ramp_sm00(tempv, bias_rng[0])


data_vs = np.zeros(tot_steps) # source voltage
data_vg = np.zeros(tot_steps) # gate voltage
data_i = np.zeros(tot_steps) # drain current


#Make Live Plots
plot1 = QtPlot()
plot1.add(data_vs, data_i, subplot=1, xlabel="Source_Voltage", xunit="V",
 ylabel= "Current", yunit ="A")
plot2 = QtPlot()
plot2.add(data_vg, data_i, subplot=1, xlabel="Gate_Voltage", xunit="V",
 ylabel= "Current", yunit ="A")


header_raw = ("Vs,_Vg,_Id")


#start Sweeping the Gate
for jj in range(bias_vsteps):
    tempv = source_read()
```

```python
        protective_ramp_sm00(tempv, bias_steps[jj]) #sets to first source bias
        print(f"Bias_Voltage:_{bias_steps[jj]}_V")
        tempv = gate_read() #read the voltage that is set
        protective_ramp_sm01(tempv, gate1_rng[0])
        for kk in range(gate1_vsteps):
            sm01.volt.set(gate1_steps[kk])
            print(f"Gate_Voltage:_{gate1_steps[kk]}_V")
            time.sleep(delay_meas)
            data_vg[jj*gate1_vsteps+kk] = gate_read()
            data_vs[jj*gate1_vsteps+kk] = source_read()
            data_i[jj*gate1_vsteps+kk] = current_read()
            plot1.update_plot()
            plot2.update_plot()
            with open(filepath+"\\data.dat", 'w') as f:
                np.savetxt(f, np.array([data_vs, data_vg, data_i]).T,
                    delimiter='\t', header=header_raw)

    print("it_took_{}_s._to_write_data".format(time.time() - t0))
    print('Ramp_to_zero')
    temp_v1 = gate_read()
    protective_ramp_sm01(temp_v1, 0)
    temp_v2 = source_read()
    protective_ramp_sm00(temp_v2, 0)

    #Turn the Keithley outputs off:
    sm00.output(0)
    sm01.output(0)
    print("Successful_Sweep--Thank_You_for_Reading_and_Have_a_Nice_Day")


if __name__ == '__main__':
    main()
```

Bibliography

[1] Momma, K. & Izumi, F. Vesta: a three-dimensional visualization system for electronic and structural analysis. *Journal of Applied crystallography* **41**, 653–658 (2008).

[2] Hull, A. W. A new method of x-ray crystal analysis. *Physical Review* **10**, 661 (1917).

[3] Novoselov, K. S. *et al.* Electric field effect in atomically thin carbon films. *Science* **306**, 666–669 (2004).

[4] Jorio, A. *et al.* Characterizing carbon nanotube samples with resonance raman scattering. *New Journal of Physics* **5**, 139 (2003).

[5] Volkov, V. & Mikhailov, S. Modern problems in condensed matter sciences (1991).

[6] Shen, G. *et al.* Toward an international practical pressure scale: A proposal for an ipps ruby gauge (ipps-ruby2020). *High Pressure Research* **40**, 299–314 (2020).

[7] Durkee, D. *et al.* Colossal density-driven resistance response in the negative charge transfer insulator mns 2. *Physical Review Letters* **127**, 016401 (2021).

[8] Van Delft, D. & Kes, P. The discovery of superconductivity. *Physics Today* **63**, 38–43 (2010).

[9] Einstein, A. Quantentheorie des einatomigen idealen gases. zweite abhandlung. *Albert Einstein: Akademie-Vorträge: Sitzungsberichte der Preußischen Akademie der Wissenschaften 1914–1932* 245–257 (2005).

[10] Anderson, M. H., Ensher, J. R., Matthews, M. R., Wieman, C. E. & Cornell, E. A. Observation of bose-einstein condensation in a dilute atomic vapor. *Science* **269**, 198–201 (1995).

[11] Novoselov, K. S. *et al.* Two-dimensional gas of massless dirac fermions in graphene. *nature* **438**, 197–200 (2005).

[12] Geim, A. K. & Novoselov, K. S. The rise of graphene. *Nature materials* **6**, 183–191 (2007).

[13] Craciun, M., Russo, S., Yamamoto, M. & Tarucha, S. Tuneable electronic properties in graphene. *Nano Today* **6**, 42–60 (2011).

[14] Craciun, M. *et al.* Trilayer graphene is a semimetal with a gate-tunable band overlap. *Nature nanotechnology* **4**, 383–388 (2009).

[15] Ferrari, A. C. *et al.* Raman spectrum of graphene and graphene layers. *Physical review letters* **97**, 187401 (2006).

[16] Cao, Y. *et al.* Unconventional superconductivity in magic-angle graphene superlattices. *Nature* **556**, 43–50 (2018).

[17] Yankowitz, M. *et al.* Tuning superconductivity in twisted bilayer graphene. *Science* **363**, 1059–1064 (2019).

[18] Trambly de Laissardière, G., Mayou, D. & Magaud, L. Localization of dirac electrons in rotated graphene bilayers. *Nano letters* **10**, 804–808 (2010).

[19] Gonzalez-Arraga, L. A., Lado, J., Guinea, F. & San-Jose, P. Electrically controllable magnetism in twisted bilayer graphene. *Physical review letters* **119**, 107201 (2017).

[20] Wolf, T. M., Lado, J. L., Blatter, G. & Zilberberg, O. Electrically tunable flat bands and magnetism in twisted bilayer graphene. *Physical review letters* **123**, 096802 (2019).

[21] Sharpe, A. L. *et al.* Emergent ferromagnetism near three-quarters filling in twisted bilayer graphene. *Science* **365**, 605–608 (2019).

[22] Song, T. *et al.* Switching 2d magnetic states via pressure tuning of layer stacking. *Nature materials* **18**, 1298–1302 (2019).

[23] Ke, F. *et al.* Large bandgap of pressurized trilayer graphene. *Proceedings of the National Academy of Sciences* **116**, 9186–9190 (2019).

[24] Zhang, Y. *et al.* Direct observation of a widely tunable bandgap in bilayer graphene. *Nature* **459**, 820–823 (2009).

[25] Castro, E. V. *et al.* Biased bilayer graphene: semiconductor with a gap tunable by the electric field effect. *Physical review letters* **99**, 216802 (2007).

[26] Tao, Z. *et al.* Raman spectroscopy study of sp2 to sp3 transition in bilayer graphene under high pressures. *Applied Physics Letters* **116**, 133101 (2020).

[27] Smith, D. *et al.* Hydrogenation of graphene by reaction at high pressure and high temperature. *ACS nano* **9**, 8279–8283 (2015).

[28] Wallace, P. R. The band theory of graphite. *Physical review* **71**, 622 (1947).

[29] Kostić, R. *et al.* Optical characterization of graphene and highly oriented pyrolytic graphite. *Acta Physica Polonica A* **116**, 718–721 (2009).

[30] Neto, A. C., Guinea, F., Peres, N. M., Novoselov, K. S. & Geim, A. K. The electronic properties of graphene. *Reviews of modern physics* **81**, 109 (2009).

[31] Young, A. F. *Quantum transport in graphene heterostructures* (Columbia University, 2012).

[32] Skrypnyk, Y. V. & Loktev, V. M. Electrical conductivity in graphene with point defects. *Physical Review B* **82**, 085436 (2010).

[33] McCann, E. Asymmetry gap in the electronic band structure of bilayer graphene. *Physical Review B* **74**, 161403 (2006).

[34] Amaral, I. *et al.* Delamination of multilayer graphene stacks from its substrate through wrinkle formation under high pressures. *Carbon* **185**, 242–251 (2021).

[35] Pacakova, B., Vejpravova, J., Repko, A., Mantlikova, A. & Kalbac, M. Formation of wrinkles on graphene induced by nanoparticles: Atomic force microscopy study. *Carbon* **95**, 573–579 (2015).

[36] Dasenbrock-Gammon, N., Dissanayake, S. & Dias, R. Pressure induced 3d strain in 2d graphene. *arXiv preprint arXiv:2207.14183* (2022).

[37] Weir, C., Lippincott, E., Van Valkenburg, A. & Bunting, E. Infrared studies in the 1-to 15-micron region to 30,000 atmospheres. *Journal of research of the National Bureau of Standards. Section A, Physics and chemistry* **63**, 55 (1959).

[38] Bassett, W. A. Diamond anvil cell, 50th birthday. *High Pressure Research* **29**, 163–186 (2009).

[39] Solin, S. & Ramdas, A. Raman spectrum of diamond. *Physical Review B* **1**, 1687 (1970).

[40] Osmond, I. *et al.* Clean-limit superconductivity in i m 3⁻ m h 3 s synthesized from sulfur and hydrogen donor ammonia borane. *Physical Review B* **105**, L220502 (2022).

[41] Nečas, D. & Klapetek, P. Gwyddion: an open-source software for spm data analysis. *Open Physics* **10**, 181–188 (2012).

[42] Haley, K. L. *et al.* Heated assembly and transfer of van der waals heterostructures with common nail polish. *Nanomanufacturing* **1**, 49–56 (2021).

[43] Berkowski, K. L., Plunkett, K. N., Yu, Q. & Moore, J. S. Introduction to photolithography: Preparation of microscale polymer silhouettes. *Journal of chemical education* **82**, 1365 (2005).

[44] Ellison, P. B., Smith, D., Sinogeikin, S. & Salamat, A. Gearbox designs for the diamond anvil cell: Applications to hard-to-reach-places (2022). URL https://arxiv.org/abs/2206.11994.

[45] Smith, D., Shelton, D. P., Ellison, P. B. & Salamat, A. Simple imaging for the diamond anvil cell: Applications to hard-to-reach places. *Review of Scientific Instruments* **89**, 103902 (2018).

[46] Snider, E. *et al.* Synthesis of yttrium superhydride superconductor with a transition temperature up to 262 k by catalytic hydrogenation at high pressures. *Physical Review Letters* **126**, 117003 (2021).

[47] Dewaele, A., Torrent, M., Loubeyre, P. & Mezouar, M. Compression curves of transition metals in the mbar range: Experiments and projector augmented-wave calculations. *Physical Review B* **78**, 104102 (2008).

[48] Xu, H., Heinzel, T. & Zozoulenko, I. Conductivity and scattering in graphene bilayers: Numerically exact results versus boltzmann approach. *Physical Review B* **84**, 115409 (2011).

[49] Sarma, S. D., Hwang, E. & Rossi, E. Theory of carrier transport in bilayer graphene. *Physical Review B* **81**, 161407 (2010).

[50] Chen, Y. *et al.* Pressurizing field-effect transistors of few-layer mos2 in a diamond anvil cell. *Nano letters* **17**, 194–199 (2017).

Curriculum Vitae

George Thomas Foskaris

georgefoskaris@gmail.com
Las Vegas, NV, USA

SUMMARY

As a graduate student of physics I have developed a deep interest in optics, electricity and magnetism, and quantum electro-dynamics. More recently, I have become fascinated by topics in condensed matter physics that pertain to metals and atomically thin materials. I am currently seeking to explore and further understand the changing properties of materials in external fields and extreme environments by developing a background in 2D physics using optical and transport methods. Beyond the research, I am driven to preserve humankinds' ability to understand the ways in which we have altered society and appreciated our world through physics and mathematics; I seek to preserve the ability to educate coming generations on some of the developments that have led us to where we are now. I believe that without an understanding of our past, we will be at a disadvantage to adapt to the future; that in the present, we must stay informed and competent in order to make real change and progress for civilization's embetterment. Doing so requires the humble confidence to challenge ourselves, each other, and approach various types of problems we face with objective, noble, and critical perspective. I find that these themes are ever present in my life and that they guide me to remain curious, modest, and push myself rigorously.

EDUCATION

GRADUATE:

M.S. in Physics, University of Nevada, Las Vegas   *November 2022 - Expected*
Thesis: *Towards the Electronic Response of Carbon-Based van der Waals Heterostructures in a Diamond Anvil Cell*
Advisors: Dr. Joshua Island & Dr. Ashkan Salamat

UNDERGRADUATE:

B.S. in Physics, University of Nevada, Las Vegas   *May 2020*
        Research: *Benchtop Fabrication of an Optical Reflectivity Spectroscopy*
                    System
        Advisor: Dr. Ashkan Salamat

EXPERIENCE

Graduate Research Assistant   *August 2020 - present*
Joint Research in the Island Nanoscale Physics Laboratory and the Nevada Extreme
Conditions Laboratory
Under Direction of Dr. Island & Dr. Salamat
University of Nevada, Las Vegas

- Currently researching the electronic response and band-structure of carbon based van der Waals heterostructures through electric field effects and pressure.

- Led the development of photolithography and electron beam deposition techniques for multi-probe electronic and/or magnetic measurements in a diamond anvil cell, whereby I performed various tests to compile an empirical methodology for the deposition of functional electrodes to the surface of a diamond.

- Two years experience developing various skills pertaining to applications of photolithography, electron beam deposition of thin-metal films, and other clean-room techniques for processing devices on various substrates, such as diamond, SiO_2, and quartz, in controlled atmospheric environments.

- Assembled and calibrated bench tops used for electronic measurements and in-situ sample microscopy.

- Over ten years experience and highly versed in image acquisition and color profiling in various software using different types of microscopes, and cameras (film or digital).

- Experience using the coding language of Python to control measurement equipment from a computer, create figures, and organize & analyze data.

- Fifteen years experience performing peer and workplace collaboration to meet common and reasonable goals.

- Three years experience and exposure to applied experimental techniques associated with various optical spectroscopy applications, such as: polychromatic reflectivity, Raman spectroscopy, microscopy, and X-Ray diffraction powder-analysis.

- Experience with high-voltage variacs and power-supplies that may be used to drive alternating currents, or ferromagnetic coils.

- Over ten years of experience using various benchtop tools and building circuits using multimeters, oscilloscopes, function generators, power supplies, various semiconductors and integrated circuits, transducers, creating PCBs, implementing frequency filters, soldering, wiring, vector analysis, imaging, problem solving, and statistical data analysis.

- Varying years of experience using various applications such as: Microsoft Office Suite, Adobe Creative Cloud, Autodesk Inventor, Autodesk CAD, Autodesk Eagle, Design CAD 2000LT, Anaconda, Express PCB, Express SCH.

- Trained in cleanroom etiquette, and the usage of various LASERs.

Graduate Teaching Assistant   *August 2020 - present*
Laboratory Physics Instructor
University of Nevada, Las Vegas

- Years of experience leading lecture, helping others, and receiving highly rated instruction of undergraduate physics laboratories on the topics of:

  - Classical Mechanics
  - Electricity & Magnetism
  - Optics

Graduate Presentation   *May 2022*
Poster: "Generating Power with Less Land"
UNLV Geosymposium

- Presented research on the energy production efficiency of different local infrastructures with respect to area and land use.

ACHIEVEMENTS

Graduate Assistantship	*Fall 2020 - Fall 2022*
American Hellenic Educational Progressive Association Scholar	*2007*
Millennium Scholar	*2007*

LANGUAGES

English
Native speaker
Spanish
Nearly fluent speaker, reader, and writer